A PHYSICOCHEMICAL PREDICTION OF PROLONGED NATURAL CO_2 LEAKAGE IN THE LITTLE GRAND WASH FAULT ZONE, GREEN RIVER, UTAH

by

Kyungdoe Han

A Thesis Submitted in
Partial Fulfillment of the
Requirements for the Degree of

Master of Science
in Geosciences

at

The University of Wisconsin-Milwaukee
May 2016

ABSTRACT

A PHYSICOCHEMICAL PREDICTION OF PROLONGED NATURAL CO_2 LEAKAGE IN THE LITTLE GRAND WASH FAULT ZONE, GREEN RIVER, UTAH

by

Kyungdoe Han

The University of Wisconsin-Milwaukee, 2016
Under the Supervision of Professor Timothy Grundl

Physicochemical investigation on a natural CO_2 system and the accommodated fault-controlled fluids using a geochemical modeling method provides important information regarding the security assessment for geological carbon sequestration (GCS), which is the most promising method for enhancing our knowledge of the side effects of GCS. By employing utilized series of regional fluid chemistry and hydrogeologic parameters, this study investigated the consequences caused by migration of CO_2 in a naturally leaking CO_2 system that developed in normal faults in the southwestern U.S. 1-D and 2-D models were conducted using the multi-phase, multi-component reactive transport simulator, TOUGHREACT, to establish sets of descriptive and interpretive data elaborating the heterogeneous water-rock-CO_2 interactions such as diagenetic quartz and phyllosilicate, and reduction of iron oxide observed on fault traces in the region. Converging evidence from silicate mineral alterations and subsurface carbonate deposits examined in the study suggest that the fault conduit has a potential to be clogged as a consequence of CO_2-bearing fluid migration. Results showed that continuous CO_2 leakage in the same location is unlikely to happen because: (i) a precipitation process involving diagenetic quartz and clay growths that are stable in the given condition of water chemistry and (ii) subsurface carbonate deposition that enhances the sealing capability of a fault zone.

Additionally, the bleaching phenomena observed in this study showed that CO_2 is the main cause of Fe mobilization in the region, without influence of methane and hydrocarbons.

To

My parents

TABLE OF CONTENTS

LIST OF FIGURES

LIST OF TABLES

LIST OF ABBREVIATIONS

1-D	One-dimensional
2-D	Two-dimensional
BBS	Big Bubbling Spring
CG	Crystal Geyser
CRG	Chaffin Ranch Geyser
Fm.	Formation
GCS	Geologic Carbon Sequestration
GRA	Green River Airport Well
Grp.	Group
k	Permeability
k_h	Horizontal Permeability
k_v	Vertical Permeability
LGW	Little Grand Wash
Mbr.	Member
PT	Pseudo Tenmile Geyser
SBS	Small Bubbling Spring
S_L	Saturation of liquid phase
SW	Salt Wash
TG	Tenmile Geyser
TS	Torrey’s Spring
TWG	Tumbleweed Geyser
yrs	years

ACKNOWLEDGEMENTS

Firstly, I would like to extend my gratitude to my thesis advisor, Dr. Weon Shik Han for his support. I would also like to thank my great committee members, Drs. Timothy Grundl and Dyanna Czeck who also provided a numerous amount of help. I have always appreciated my committee members' never-ending enthusiasm and their priceless help. It was really honorable to get precious insights from all of my professors above.

Most of the staffs and students at the UWM have aided me. I would also like to thank my lab mates, Ethan Guyant, Emily Joynt, Zach Watson, Jack Graham, Cassandra Wolf, and John Teppler. I appreciate Megan Barlow, for spending a lot of time listening to my researches and whining. Kate Pauls and Emily Joynt for their help about writing. I thank Ken Oanes for taking me home when I passed out. I also thank Kurt Quamme, Levi Moxness, Abuduwufu Patiman and Devin Gerzich for their good advice.

My special thanks go toward Carolyn Kim for her warmest support and much needed guidance on organizing my paragraphs in context.

This research was aided by the generous scholarships from UW-Milwaukee and Wisconsin Geological Society.

This thesis might comprise of idea and thought that were developed in my tiny little closet-like office, however, I could never finish without kind support of the aforementioned nicest people in the Cream City. My final gratitude goes toward my parents and my brother.

Kyungdoe Han

1. Introduction

Geologic carbon sequestration (GCS) has been considered an adequate method of segregating CO_2 from the atmosphere for the purpose of reducing the emission of greenhouse gases (Reichle et al., 1999). During the process of GCS, CO_2 is disposed into a target brine (saline) storage aquifer from large fixed sources such as fossil-fuel power stations. CO_2 that is injected to the subsurface storage aquifer may encompass an expansive areal extent over a long time-scale targeting more than 10,000 yrs. (e.g., over 10 km in linear dimension or further; Pruess et al. (2001)). Such a developed CO_2 plume with a long migration history could have potentials to encounter geologic imperfections such as fault zones or fractures, which would allow CO_2 to escape from primary storage aquifers into upper shallow regional groundwater systems (Pruess, 2008).

Thus, despite their efficacy and efficiency, the possibility of CO_2 leakage near injection sites is a major drawback to emerging GCS projects. Numerous concerns arise due to potential hazards associated with CO_2 discharge through preferential pathways to the surface. These include (1) potential groundwater contamination caused by water-rock interactions by acidic and corrosive characteristics of CO_2-laden fluid (Apps et al., 2010; Atchley et al., 2013; Carroll et al., 2009; Czernichowski-Lauriol et al., 1996; Gunter et al., 1997; Kharaka et al., 2010; Siirila et al., 2012; Wang and Jaffe, 2004; Wilson et al., 2007); 2) asphyxiation of animal species caused by a dense gaseous CO_2 accumulation on the land surface, for example, Mammoth Mountain, CA, USA (Lewicki et al., 2007) and Lake Nyos, Cameroon (Kling et al., 1987; Kusakabe et al., 1989); and 3) the decrease of storage efficiency while the GCS targets a long period of time for the containment of CO_2 in reservoirs, more than thousands of years (Bachu et al., 1994; White et al., 2005).

It may be inferred that the most probable leakage pathways could be sub-vertical faults and fracture zones that have not been identified during the characterization of GCS sites, connecting the target storage reservoir and land surface (Person et al., 2007; Pruess, 2008). Since a fault zone, in general, exhibits various geologic imperfections that allow fluids to make headway (fracture segments and damage zones), a focused channel for fluid flow can be formed in any given fault zone architecture (Anderson and Fairley, 2008; Eichhubl et al., 2009; Matthäi and Belayneh, 2004).

Hence, enhancing our knowledge about leaking CO_2 and the relevant changes induced by CO_2 in such fault zones will help to assess the long-term security of GCS and gain public acceptance. A considerable amount of literature has discussed the escape of CO_2 through geologic imperfections in an effort to evaluate the long-term security of GCS (Burnside et al., 2013; Chang et al., 2008; Chiaramonte et al., 2008; Lewicki et al., 2007; Lu et al., 2012; Oldenburg and Lewicki, 2006; Pruess, 2005; Pruess, 2008; Rinaldi et al., 2014; Shipton et al., 2004). From the above previous studies, the following are suggested for study in order to assist a selection of appropriate storage sites and achieve safer storage conditions for CO_2 leakage: 1) changes in properties of CO_2 and reservoir fluids (i.e., brine) during its migration along faults and fractures; 2) numerical modeling that exhibits a realistic leakage scenario with chemical changes induced by water-rock-CO_2 interactions; and 3) investigations on natural analogues such as natural CO_2 reservoirs and CO_2-leaking faults.

Only a handful of studies, however, are able to quantify the hypothetical CO_2 leakage through geologic imperfections and obtain empirical evidence from the leakage phenomena in natural analogues (Ennis-King and Paterson, 2002; Pruess, 2008; Pruess and Garcia, 2002; Rutqvist and Tsang, 2002; Shipton et al., 2004). The conducted numerical modeling studies in hypothetical CO_2 leakage systems have provided the quantitative and mechanical understanding of flow behavior. It has been suggested that natural analogues can provide crucial evidence regarding geochemical processes that will contribute to adjust the existing numerical models (Gherardi et al., 2007; Haszeldine et al., 2005).

Therefore, this study sought to examine the CO_2-rich natural environment with the currently ongoing leakage phenomena to overcome the practical constraints of modeling, by implementing field-based geologic parameters on reactive transport simulations. The research site that was investigated is a naturally leaking CO_2 system, which revealed anomalous CO_2 flux (i.e., diffusive leakage) and eruptive CO_2 emission (i.e., advective leakage) adjacent to normal faults in Utah. The principal focus of examination is the water-rock interaction with gaseous CO_2 that would be promoted by CO_2 migration through a fault conduit residing in the region. Implemented site-specific fluid chemistry data were collected from 1965 to 2014 (Baer and Rigby, 1978; Barton and Fuhriman, 1973; Heath et al., 2009; Kampman et al., 2014; Kharaka et al., 1997; Shipton et al., 2004; Spangler, 1992; Watson et al., Submitted Article). Applied mineral abundances, fault geometry, and formation settings followed previously observed data on the study area (Allis et al., 2001; Burnside, 2010; Hanshaw and Hill, 1969; Hansley, 2000; Hintze, 1993; Hood and Patterson, 1984; Jung et al., 2015; Trimble and Doelling, 1978; White et al., 2003; Zuluaga et al., 2014).

From the investigations made in this study, the following key issues were examined in terms of quantitative results from the series of multi-phase reactive transport models: 1) the alterations of minerals inducing physical and chemical changes in a fault conduit by coupled heterogeneous reactions (i.e., dissolution and precipitation of minerals); 2) a potential connectivity of the cold water geyser system with subsurface CO_2 distribution along the fault structure and geometry; and 3) a cause of *in-situ* mobilization and deposition of iron-bearing minerals with correlations to field observations.

Understanding the multi-phase flow behavior and reactive transport mechanism resulting from water-rock interactions under a naturally leaking CO_2 system, as seen in the results of this study, can provide information to assess the long-term security of GCS and in turn, gain public acceptance.

2. Research Site Description

2.1. Regional Geology

The Greater Colorado Plateau area is a slightly elevated tectonic block which encompasses 390,000 km^2 throughout the Four Corners region of UT, CO, AZ, and NM (Stewart et al., 1972; Fig. 1a). The plateau has distinct natural resources: 1) hydrocarbon potentials (Baars, 1966; Baker, 1933; Brandt, 1987; Hansley, 2000; Nuccio and Condon, 1996), 2) mineral resources (e.g., Potash salts, Cu and Ag ores; Hite and Gere, 1958; Morrison and Parry, 1986), and 3) naturally occurring CO_2 fields with an estimated CO_2 storage of over 28×10^9 to $2{,}800 \times 10^9$ m^3 (Allis et al., 2001). The connatural CO_2-rich fields in the region are mostly sealed laterally toward the fault center by anticlines, which are compartmentalized with a dome-type four-way anticlinal closure or fault seals (Shipton et al., 2004). In this region, the CO_2 fields contain gases dominated by CO_2 (up to 98 vol. %). These CO_2 reservoirs (e.g., Gordon Creek, Farnham Dome, Lisbon and McElmo Dome fields; Fig. 1) were economically developed to be used in the process of CO_2 enhanced oil recovery and dry ice production (Allis et al., 2001; Cappa and Rice, 1995; Dobbin, 1969; Gerling, 1983; Walton, 1955).

The intraforeland flexural Paradox Basin associated with the Uncompaghre Uplift is positioned at the northwest boundary of the Colorado Plateau, trending asymmetrically NW-SE with an accumulation of thick carbonates, halite and clastic deposits (Barbeau, 2003; Nuccio and Condon, 1996; Fig. 1a). The region is a part of the intracratonic basin associated with the ancestral Rocky Mountains (Dickinson and Lawton, 2003; Trudgill, 2011). The border of the basin characterizes the total extent of the salt in the Paradox Formation (Fig. 1b; Hite, 1968; Shipton et al., 2004). The stratigraphy of the basin spans from the Pennsylvanian Paradox Formation to the Mid-cretaceous Mancos Shale (Dockrill and Shipton, 2010). In addition, this thick Paleozoic sediment reflects a high subsidence rate of the basin, showing an alternating sequence of shallow and deep marine depositional environments (Barbeau, 2003).

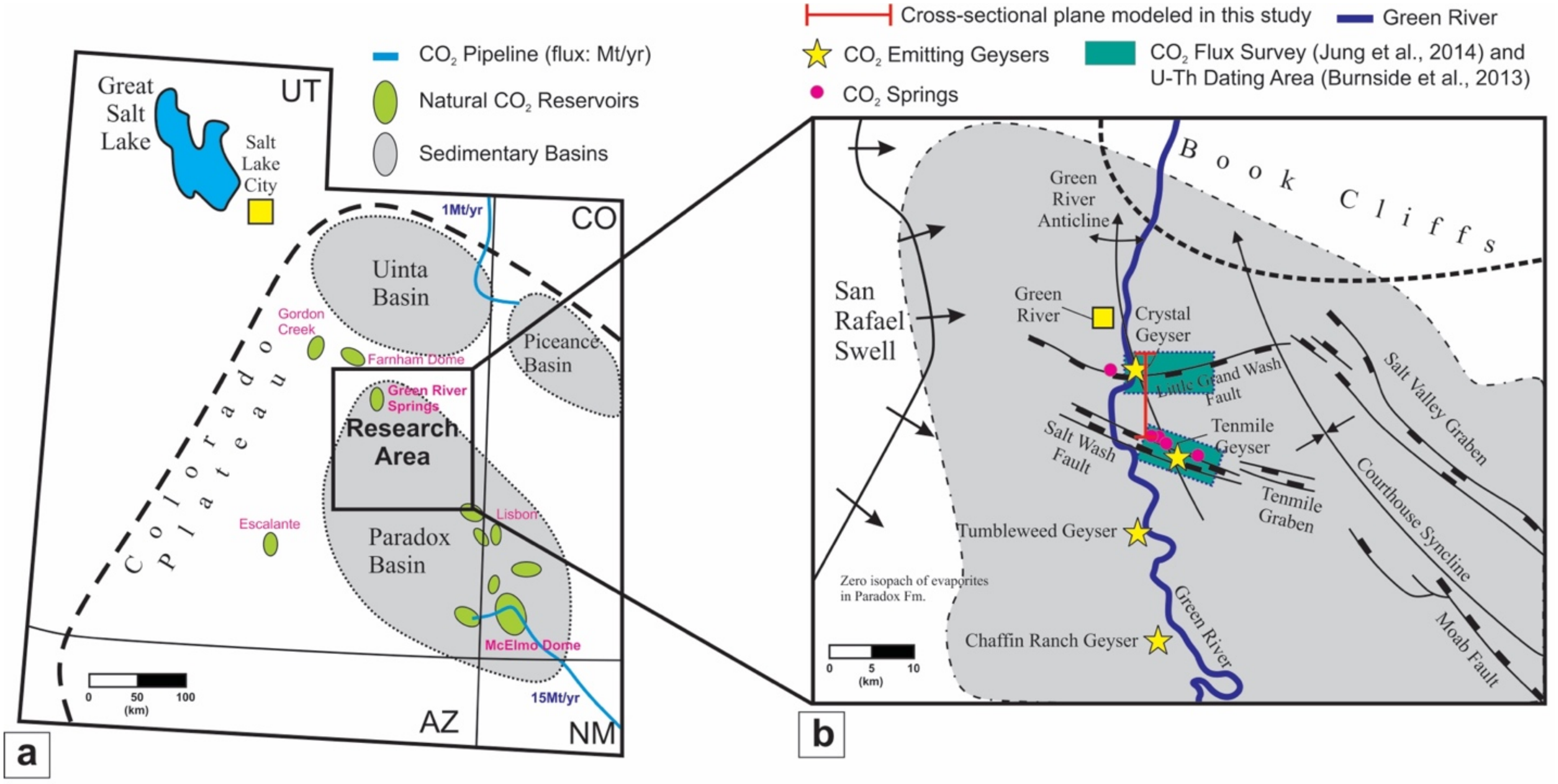

Figure 1. Map of the research area. (a) Areal view of the Paradox Basin including natural CO_2 reservoirs and commercial CO_2 pipelines (modified from Allis et al., 2001). (b) Geologic map of the research area, the northwest corner of the Paradox Basin (redrawn from Dockrill, 2006).

2.2. The Little Grand Wash (LGW), Salt Wash (SW), and Moab Fault systems

Fault systems in the Paradox Basin developed in the Permian age due to the regional elongation of the basin and reactivated again by Sevier and Laramide orogenies from Cretaceous and Oligocene periods (Pevear et al., 1997; Solum et al., 2010; Chan et al., 2000). During the deformation of the basin, faulting was concentrated throughout the margin of valleys residing along the crests of salt anticlines, which caused highly diffuse deformation in the area, e.g., warping, tilting, and deformation of valley-fill deposits (Hecker, 1993). Evidence provided by local earthquakes indicates that the stress regime of the region could be characterized by a NW-trending horizontal extension, although there are low differential stresses and variances in the magnitude of seismicity (Zoback and Zoback, 1989). In addition, the currently active uplift of the Colorado Plateau maintains the region under an extensional stress regime (Frery et al., 2015). Finally, the mobility and solubility of halite deposits in the basin caused a series of Cenozoic dissolutional collapses which indicates that faults retain the potential for local and regional seismicity. This is supported by field observations of distinct NW oriented faults in the western Colorado plateau (Hecker, 1993).

The Little Grand Wash (LGW) and the Salt Wash (SW) normal faults are situated adjacent to the town of Green River, UT (Fig. 1b), cutting the northern outskirts of the Paradox Basin. The east-west striking LGW fault intersects the north- to northwest plunging Green River anticline (Dockrill, 2005; Shipton et al., 2004). The fault is extended approximately 30 km, showing a 70° dip-slip to south. The fault slip varies by the location (Dockrill and Shipton, 2010a; Dockrill and Shipton, 2010b; Williams, 2005), but its major offset consists of Jurassic Morrison members and Cretaceous Mancos Shale (Table 1). The maximum fault throw appears to be 260 m proximate to the Crystal Geyser (Fig. 2a) and gradually declines toward the east- and west-ends of the LGW fault. At the surface, the LGW fault juxtaposes late Jurassic formations (e.g., Morrison, Summerville, and Curtis) on the northern footwall with Cretaceous (e.g., Mancos shale) formations on the southern hanging wall. Despite uncertainties of subsurface information, lithologic data from Amerada Hess wells #1 and #2 revealed that the fault may penetrate deep into the Pennsylvanian-aged formation (Dockrill and Shipton, 2010a) where halite is abundant (Nuccio and Condon, 1996) consists of two parallel strands with an average width of 800 m dips southward at an average of 73° (Dockrill and Shipton, 2010a; Dockrill and Shipton, 2010b).

The SW fault has a graben over 23 km along the strike of the fault while the offset of the fault cuts the north plunging Green River Anticline (Fig. 1b). The northern SW fault has a dip of 78° S and the southern fault has a dip of 87° N (Williams, 2005). The maximum offset across the northern and southern faults is 366 m and 210 m, respectively. At the northern footwall, the bleached Jurassic Entrada Sandstone is exposed at the surface while the Cretaceous to Jurassic Cedar Mountain Formation is exposed at the surface on the southern SW graben (Table 1; Wigley et al., 2012).

To the east-end of the SW fault, the Tenmile Graben extends over 9 km (Williams, 2005; Fig. 1b). Geometric complexities through the fault traces and variations in the throw along the strike imply there is a linkage of kinematic movement between the Tenmile Graben and the SW Fault system (Dockrill and Shipton, 2010a; Dockrill and Shipton, 2010b). Reservoir-scale faults (Moab and Salt Valley faults) which penetrate the entire Paradox formation are located further east (Doelling et al., 1988; Foxford et al., 1998). The Moab Fault is a 45 km-long normal fault system (Doelling, 1985; Foxford et al., 1996), with three main constituents: 1) the southern section with poor exposure; 2) the central section with the greatest throw (~1km); and 3) the northern section with complex branches (Solum et al., 2010).

Constraining the timing of continued movement of the Moab and Salt Valley faults is difficult although early Tertiary and Quaternary slips were discovered by trenching on those faults (Pevear et al., 1997; Williams, 2005). The consistent dissection of Mancos Shale throughout surficial fault traces coevals with the fault activity that occurred at least up to the Mid-Cretaceous period (Vrolijk et al., 2005) while fault-related diagenesis and the K-Ar dating results of shale gouge in the Morrison Formation indicate that the faulting occurred between 60 and 43 Ma (Davatzes and Aydin, 2003; Pevear et al., 1997). Even though there is no direct evidence, both the SW fault and Tenmile graben could potentially penetrate to the Paradox Formation based on their geographical proximity to these large fault systems.

Table 1. Stratigraphy of the Green River area where Grp., Fm., and Mbr. stand for group, formation and member, respectively. Data were obtained from Trimble and Doelling (1978); Hintze (1993); Hanshaw and Hill (1969); Hood and Patterson (1984). Shaded portions of the table represent major CO_2-sourcing and CO_2-charged aquifers.

Age	Group	Formation and Member		Thickness (m)
Cretaceous		Mancos Shale	Upper Shale	200 +
			Ferron Sandstone	6 - 10
			Tununk Shale	105 - 125
		Dakota Sandstone		0 - 10
		Cedar Mountain Formation		45 - 55
		Buckhorn Conglomerate		0 - 10
Jurassic		Morrison Formation	Brushy Basin Member	70 - 146
			Salt Wash Member	45 - 90
			Tidwell Member	6 - 15
	San Rafael	Summerville Fm.		30 - 120
		Curtis Fm.		40 - 70
		Entrada Sandstone		120 - 145
		Carmel Fm.		65 - 90
	Glen Canyon	***Navajo Sandstone***		130 - 155
		Kayenta Fm.		58 - 73
		Wingate Sandstone		90 - 120
Triassic		Chinle Fm.	Church Rock Mbr.	60 - 120
			Moss Back Mbr.	16 - 30
			Temple Mountain Mbr.	0 - 12
		Moenkopi Fm.	Moody Canyon & Torrey Mbrs.	140 - 200
			Sinbad Limestone Mbr.	10 - 15
			Black Dragon Mbr.	50 - 65
Permian	Cutler Grp.	Kaibab Limestone		0 - 45
		White Rim Sandstone		90 - 150
		Organ Rock Shale		0 - 90
		Elephant Canyon		300 - 365
Pennsylvanian	Hermosa Grp.	Honaker Trail Formation		150 - 300
		Paradox Formation		365 - 760
Mississippian		***Leadville Limestone***		185 - 245

2.3. Evidence of Fault Leakage Phenomena

The abundance of subsurface CO_2 in the region is reflected on the surface as travertine deposits. At the center of the LGW fault, two strands (northern and southern traces) extend 3.2 km east and 0.1 km west to the Green River (Fig. 2a). The active travertine deposit appears a few meters north of the LGW fault where the Crystal Geyser periodically emits effluents. In contrast, a stratigraphic succession of inactive travertine deposits appears alongside geologic imperfections (e.g., faults and fractures; Barth, 2012; Doelling, 1994; Gratier et al., 2012). Currently, the inactive travertines are topographically higher than the active travertine. Recently, the U-Th age dating results of the travertine mounds revealed that CO_2 has leaked for at least 113,900 yrs along the LGW fault and 413,000 yrs along the SW fault (Fig. 2a and 2b; Burnside et al., 2013).

The exposure of the bleached red-bed Entrada sandstones at the northern footwall of the SW fault shows further evidence of CO_2-rich fluid leakage (Fig. 2c). Regional burial diagenesis has developed Fe-oxide grain coatings in the Jurassic Entrada sandstones, giving the perceptible reddish color (Cullers, 1995; Trimble and Doelling, 1978; Wigley et al., 2013b). Petrological alterations (e.g., dissolution of Fe-oxide grain coatings and K-feldspar) induced by acidic dissolution reactions of CO_2-rich brine at low pH are considered to be a cause of bleaching in the Entrada Formation (Wigley et al., 2013b). Bleached Entrada sandstones are also observed at drilled in-situ cores from the CO_2W55 well located at 90 m north of LGW fault trace and 285 m west of the Crystal geyser (Kampman et al., 2014). In addition, distinctive iron oxide reduction and pyrite cementation are observed in the Moab Fault zone (Foxford et al., 1996).

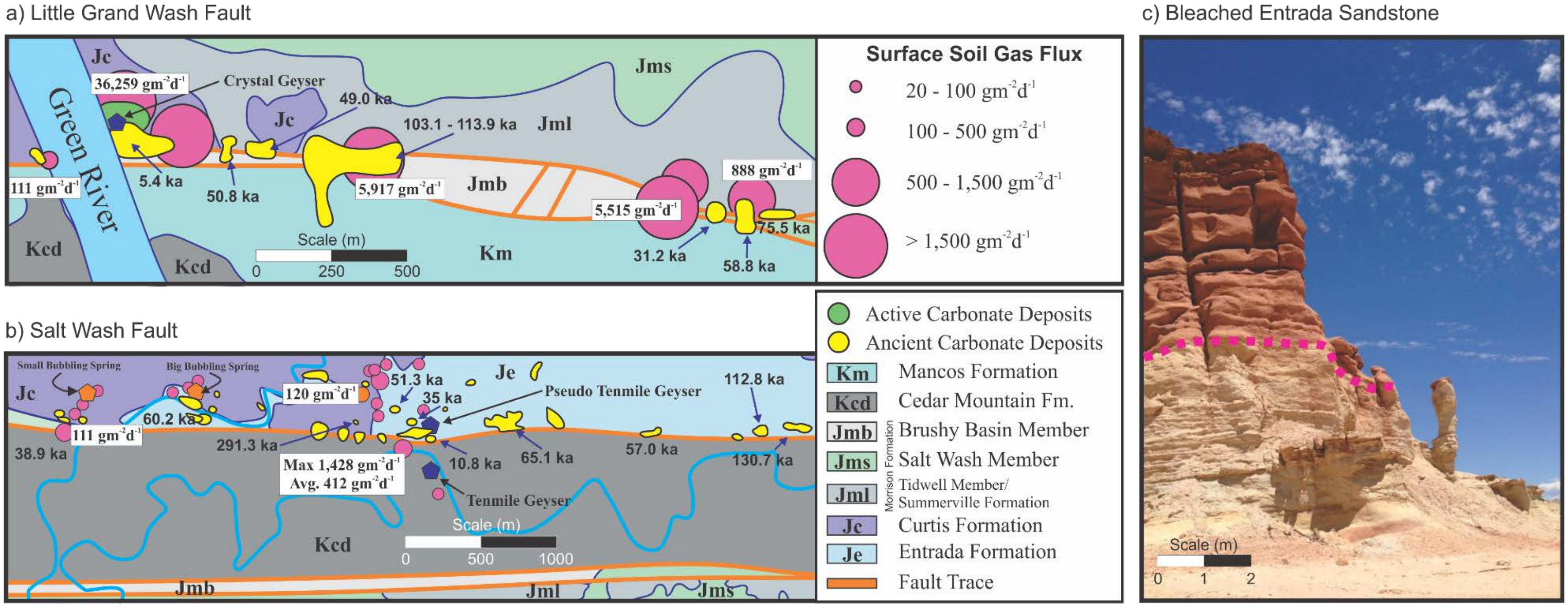
a) Little Grand Wash Fault

b) Salt Wash Fault

c) Bleached Entrada Sandstone

Figure 2. Geologic map of the Little Grand Wash and Salt Wash fault zones overlapped with surveyed soil CO_2 flux data [g m^{-2}d^{-1}] from Jung et al. (2014) and travertine deposits from Burnside et al. (2010); (a) Little Grand Wash Fault, (b) Salt Wash Fault and (c) bleached Entrada Sandstone adjacent to the Tenmile Geyser.

A series of advective-diffusive CO_2 flux anomalies above the fault traces and cold-water geysers/springs also show active leakage of faults (Allis et al., 2001; Han et al., 2013; Jung et al., 2014). Highly anomalous CO_2 fluxes were observed specific to the northern footwall of both LGW and SW faults, and the adjoining locations of two fault strands where massive travertine deposits exist (Fig. 2a and b). Furthermore, unnaturally leaking artificial wells such as Crystal and Tenmile geysers were developed following traces of LGW and SW faults (Figs. 1b, 2a and 2b). Other carbonate springs (e.g., Torrey's Spring, Big Bubbling Spring, and Small Bubbling Spring) chiefly located along the northern footwall of the SW fault trace (Baer and Rigby, 1978; Campbell and Baer, 1978; Doelling, 1994) emit both CO_2 and brine from CO_2-bearing formations (e.g., Jurassic Entrada and Navajo sandstones). In addition, a fresh hydrocarbon seep east of the Crystal Geyser shows evidence of reductive fluid migration to the surface (Shipton et al., 2004).

Seismic activities that are likely to be associated with the study area can affect the leakage behavior of the CO_2-laden fluid. Earthquake-induced changes in a stress field are a cause of hydrologic variations including fluctuation of fluid and gas flux (Elkhoury et al., 2006). Deformation by static stress change can induce changes in pore pressure and in the amount of pore fluid (Manga and Wang, 2007). In short, dynamic stress variation on sandstones in the area can cause an opening and closing of preferential pathways for migrating fluids by oscillating pore pressures and changes in permeability (Liu and Manga, 2009; Elkhoury et al., 2006; Petit et al., 1999; Renard et al., 2000).

2.4. CO_2 Origin

Various processes can yield CO_2 from source rocks in basin structures, e.g., carbonate metamorphism, hydrocarbon maturation, mantle degassing, and organic activities (Selley and

Sonnenberg, 2014). Former studies suggested possible scenarios for CO_2 generation in this area: 1) clay-carbonate reactions in the Paradox Formation (Dockrill and Shipton, 2010a; Heath et al., 2009), 2) thermal decomposition of Leadville Limestone by the Tertiary intrusions of the Henry and La Sal Mountains (Cappa and Rice, 1995; Shipton et al., 2004; Wilkinson et al., 2008), 3) thermal decomposition/maturation of kerogen and hydrocarbon (Cappa and Rice, 1995; Shipton et al., 2004), and 4) transportation of CO_2 into the crust by igneous intrusions (Ross, 1998; Wilkinson et al., 2008). One hypothesis cannot solely describe the mechanism for CO_2 production in this region, but researchers generally agree that the Mississippian Leadville Limestone and the Paradox Formation are potential sourcing formations (Table 1).

Carbon isotope ratios ($\delta^{13}C$ in V-PDB; Vienna Pee Dee Belemnite) of gaseous CO_2 bubbles ranges from -6.5 to -8.5 ‰ V-PDB at Green River springs (Wilkinson et al., 2008) and -5.7 to -7.6 ‰ V-PDB at the Crystal Geyser area (Jeandel et al., 2010), respectively, which fall within the ranges of both bulk crustal- and mantle-originated carbon (Bulk crustal: -5 to -7‰ V-PDB and Mantle: -3 to -8‰ V-PDB) without indication of biologically originated carbon (Frery et al., 2015; Wilkinson et al., 2008). Due to no distinction of $\delta^{13}C$ ratios indicating the source of CO_2, previous studies relied on analyzing ratios of $^3He/^4He$ and $CO_2/^3He$ to determine the sources (Heath et al., 2009; Wilkinson et al., 2008). Initially, Heath et al. (2009) reported that $^3He/^4He$ ratios were 0.302 and 0.310 at the Crystal Geyser and the Big Bubbling Spring, respectively, suggesting that degassing from the mantle or magma is not the major source although later Wilkinson et al. (2008) noted that these data might be contaminated with air. Alternatively, Wilkinson et al. (2008) suggested a source-tracking method using the $CO_2/^3He$ ratio, by assuming that this ratio is conserved while CO_2 migrates to the surface. Considering the mantle-originated $CO_2/^3He$ ratio to be 1×10^9 to 6×10^9 (Marty and Jambon, 1987), the $CO_2/^3He$ ratio data ranging from 1.4×10^{10}

to 6.4×10^{12} in these geyser/springs indicate that CO_2 originated dominantly from the crust. Therefore, supported from the fact that the Green River area was the most thermally matured zone in the Paradox basin, thermal decomposition of Leadville Limestone activated by tertiary tectonic events is considered to be the sourcing mechanism of CO_2 (Gilfillan et al., 2008; Nuccio and Condon, 1996; Wilkinson et al., 2008).

Table 2. Averaged chemistry data of the Green River Springs (CO_2-emitting springs and geysers). Data were adapted from [§]Watson et al. (submitted article), [¶]Barton and Fuhriman (1973), [Ӿ]Kampman et al. (2014), [†]Baer and Rigby (1978), [‡]Shipton et al., (2004), [£]Heath et al. (2009), and this study. *Stdev. stands for the standard deviation of averaged samples.

Location	Temperature ºC	Stdev. (T)	pH (in situ)	Stdev (pH)	Alkalinity mEq/L	Stdev. (Alk.)	TDS mg/L	Stdev. (TDS)	Number of Samples	References
Green River Airport Well (GRA)	26.80	-	6.28	-	37.08	-	6058	-	1	Ӿ
Crystal Geyser (CG)	16.64	1.34	6.79	0.12	71.14	8.64	15,009.65	1182.42	72	§¶Ӿ†
Small Bubbling Spring (SBS)	16.50	3.82	6.28	0.06	59.11	2.45	15426.5	65.62	5	§£Ӿ
Big Bubbling Spring (BBS)	16.50	1.69	6.39	0.04	68.51	2.09	19098.9	742.32	3	§£Ӿ
Tenmile Geyser (TG)	15.65	4.03	6.51	0.06	58.76	1.66	18123.37	940.75	4	§Ӿ‡
Pseudo Tenmile Geyser (PT)	15.00	1.13	6.45	0.04	63.95	1.37	19669.2	237.02	4	§Ӿ£
Torrey's Spring (TS)	15.80	0.85	6.53	0.03	81.06	1.61	22223.35	1164.11	5	§Ӿ£‡
Tumbleweed Geyser (TWG)	17.90	1.09	6.30	0.06	63.02	2.11	17818.3	601.98	3	Ӿ‡£
Chaffin Ranch Geyser (CRG)	16.00	-	6.25	-	77.26	-	18556.4	-	1	Ӿ

Table 3 (continued). Averaged chemistry data of the Green River Springs (CO_2-emitting springs and geysers). Data were adapted from [§]Watson et al. (submitted article), [¶]Barton and Fuhriman (1973), [⁎]Kampman et al. (2014), [†]Baer and Rigby (1978), [‡]Shipton et al., (2004), [£]Heath et al. (2009), and this study. *Stdev stands for the standard deviation of averaged samples.

Location	Ca^{2+} mmol/l	Stdev. (Ca^{2+})	K^+ mmol/l	Stdev. (K^+)	Mg^{2+} mmol/l	Stdev. (Mg^{2+})	Na^+ mmol/l	Stdev. (Na^+)	Cl^- mmol/l	Stdev. (Cl^-)	SO_4^{2-} mmol/l	Stdev. (SO_4^{2-})
(GRA)	22.20	-	2.20	-	8.80	-	20.50	-	3.70	-	8.51	-
(CG)	24.81	1.91	8.31	0.82	9.10	1.12	154.60	17.10	105.30	13.73	22.05	2.63
(SBS)	21.96	3.05	9.16	0.51	10.16	0.92	179.45	20.72	119.85	11.10	25.63	4.91
(BBS)	24.34	1.61	11.23	0.25	9.79	0.69	233.50	21.49	156.80	22.34	29.60	6.79
(TG)	23.01	2.15	6.67	0.94	8.81	1.97	217.18	15.33	184.63	15.80	21.10	4.69
(PT)	22.16	2.06	11.48	0.11	9.15	0.92	246.90	32.67	166.55	17.75	31.89	5.95
(TS)	27.58	3.08	13.50	0.14	8.98	0.82	275.70	40.02	197.35	31.61	26.85	12.81
(TWG)	28.30	2.14	8.60	0.31	10.30	0.75	192.70	24.81	154.90	19.06	29.60	5.95
(CRG)	27.60	-	8.60	-	10.30	-	194.20	-	154.80	-	29.90	-

3. Geochemical Observations

3.1. Sample Collection and Compilation

Analyses of pH, alkalinity, total dissolved solids (TDS), temperature, and dissolved concentration of species were conducted in this study. Water chemistry data consisting of 98 entries were compiled to establish a reference chemistry dataset (Barton and Fuhriman, 1973; Heath et al., 2009; Hood and Patterson, 1984; Kampman et al., 2014; Kharaka et al., 1997; Shipton et al., 2004; Spangler, 1992; Watson et al., Submitted Article). The samples for water chemistry analysis were collected from 4 geysers and 4 springs, the Green River Airport Well, the CO_2W55 drilling site and 5 brine sources from former studies. Crystal Geyser effluent samples were collected in Dec. 2010, May/June 2013, and May/June 2014 (Watson et al., Submitted Article).

3.2. Characteristics of Regional CO_2-rich Fluid Chemistry

In the study area, eolian sandstones that are mostly composed of quartz arenite serve as reservoirs for a CO_2-charged groundwater system with high porosity and permeability (Hintze, 1993; White et al., 2005; Burnside, 2010). Formerly, the porosity of the Navajo Sandstone was measured up to 26.8 % (Hood and Patterson, 1984). In addition, the recently calculated porosity of the Navajo and Entrada sandstones were 19.5% and 26.4%, respectively, showing a high potential for rapid fluid motion inside the sandstones (Burnside, 2010).

The regional chemistry of CO_2-rich fluid are expressed by Stiff diagrams, which were drawn with a compiled dataset of Green River Springs (i.e., CO_2-emitting springs and geysers). Major ionic concentrations were averaged by a total number of samples at each location (Fig. 3).

In addition, *in-situ* formation water chemistry data collected during the CO_2W55 drilling project was also plotted (Kampman et al., 2014). The Green River Airport (GRA) well, which is located at the west-end of the LGW fault closest to the San Rafael Swell, is considered to be the closest approximation of meteoric water source of the area (Kampman et al., 2014). Following eastward over the trace of LGW fault, water chemistry from both the CO_2W55 well and the Crystal Geyser (CG) show the elevated concentration of Na^+ and Cl^-, indicating an influx of deeply sourced brine. Further south of the LGW fault, Big Bubbling spring (BBS), Small Bubbling spring (SBS), Pseudo-Tenmile Geyser (PT), Tenmile Geyser (TG), and Torrey's Spring (TS), which are located at the northern footwall of the SW fault and within the SW Graben (Fig. 3), emit even more saline effluent. The elevated concentration in the SW springs suggests the contribution of brine influx into the fault could be larger at the SW fault than the LGW fault. Further south, the Tumbleweed (TWG) and the Chaffin Ranch geysers (CRG), which are not directly above the fault systems, show continuous bubbling and intermittent eruptions, respectively. Although these geysers are positioned relatively distant from the SW fault, they still show comparable fluid chemistry to the SW springs (Fig. 3).

Overall, concentrations of major cations for all CO_2 geysers/springs show $Na^+ > Ca^{2+} > Mg^{2+} > K^+$, and anions for $Cl^- > HCO_3^- > SO_4^{2-}$, respectively (Table 2).

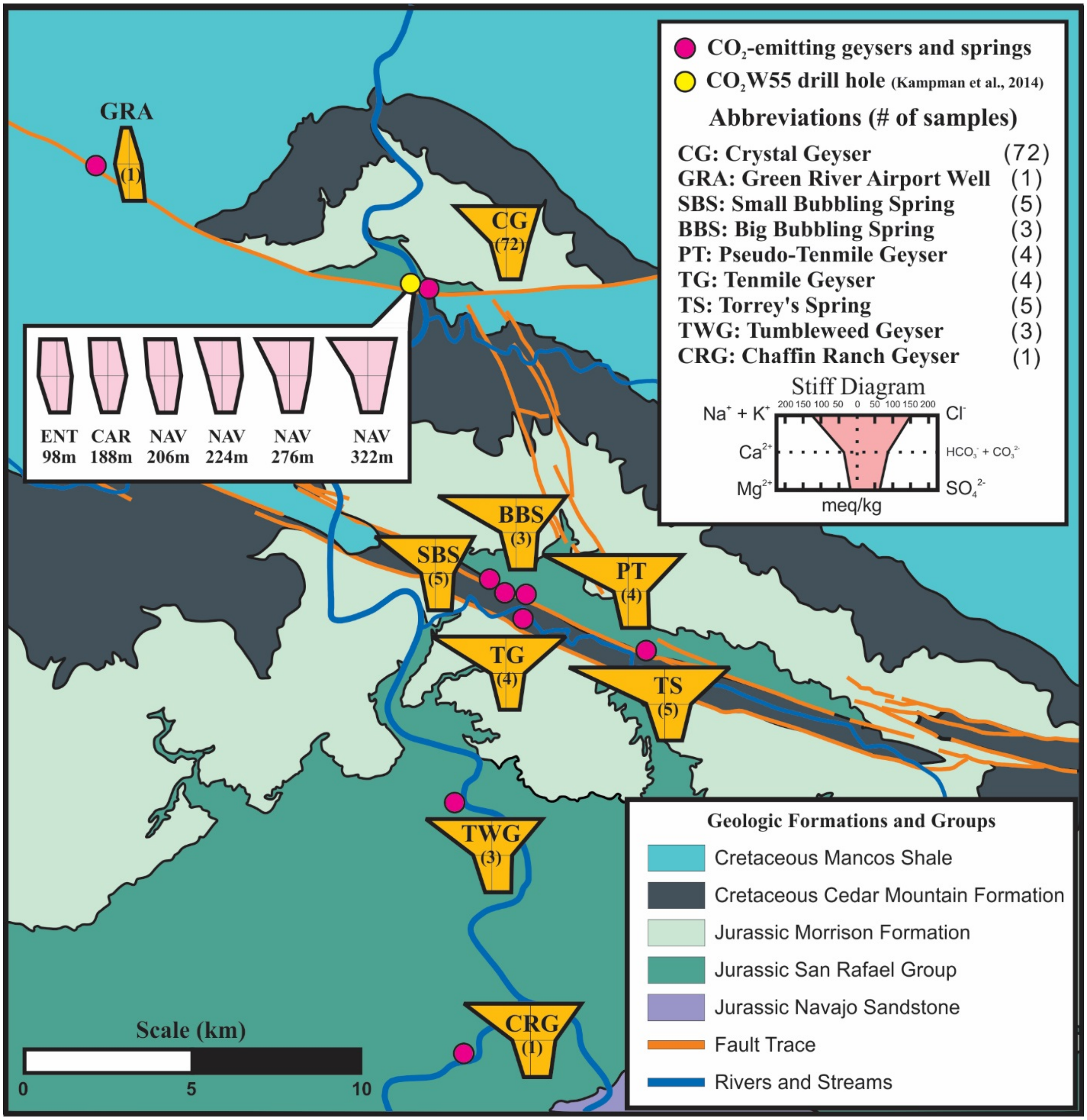

Figure 3. Geologic map of the Green River area overlying Stiff diagrams from CO$_2$ emitting springs and geysers; a geologic map was redrawn after Kampman et al. (2014). Orientation of formation boundaries depict the anticlinal structure of the region. The Stiff diagrams were plotted with total 93 samples compiled from Kampman et al. (2014), Shipton et al. (2004), Heath et al. (2009) and this study. Concentrations of major ions were averaged with the number of samples available at each location. Abbreviations of each unit follows Entrada Sandstone (ENT), Navajo Sandstone (NAV), Green River Airport Well (GRA), Crystal Geyser (CG), Small Bubbling Spring (SBS), Big Bubbling Spring (BBS), Tenmile Geyser (TG), Pseudo Tenmile Geyser (PT), Torrey's Spring (TS), Tumbleweed Geyser (TWG), and Chaffin Ranch Geyser (CRG).

3.3. Characteristics of Fluid End-members and Evolution to the Green River Springs Effluents

The aquifer system in the Paradox Basin was formerly classified into two categories: 1) the Shallow Jurassic Aquifers, consisting of permeable sandstones of the Entrada, Navajo, and Wingate Formations (Naftz et al., 1997), and 2) the Deep Paleozoic Aquifer influenced by the evaporites in the Paradox Formation (Rush et al., 1982). The Jurassic Navajo and Entrada Sandstones serve as major sources of CO_2-unsaturated groundwater, due to their massive areal extent and thickness of formations (Hood and Patterson, 1984). The carbonate and salt species dissolved in brine presumably originated from the Mississippian Leadville Limestone and Pennsylvanian Paradox Formation, respectively (Table 1; Kampman et al., 2014; Wilkinson et al., 2008).

These two fluid end-members, the Shallow Jurassic and Deep Paleozoic Aquifers, currently contribute to the ambient fluid chemistry within the fault zones, and consequently, the effluents of Green River Springs are evolved from mixtures of these two end-members. A modified Durov diagram presents this systematic evolution of mixed fault fluids (Fig. 4). Group I (pink) characterizes the Shallow Jurassic Aquifers that delineates the transition of fluid chemistry from Na^+-HCO_3^--typed to Na^+-Cl^--typed groundwater as the depth is increased from the Entrada, Carmel, to Navajo Formations (Fig. 4); for example, salinity notably increases from the Entrada Sandstone at 98 m ($Na^+ + K^+$: 39.9% and Cl^-: 24.9%) to the Navajo Sandstone at 322 m ($Na^+ + K^+$: 63.6% and Cl^-: 44.7%). Overall, the pH and TDS of the Shallow Jurassic Aquifers range from 5.1 to 6.3, and from 8,186.0 to 13,254.8 mg/L, respectively, revealing the most acidic and least dissolved solid concentration relative to the other end-member fluids (see plane for TDS vs. pH). In addition, concentration of carbonate species ($HCO_3^- + CO_3^{2-}$) within the Shallow Jurassic

Aquifers is the highest among the groups (Table 3), which indicates accumulation of CO_2-charged brine.

Finally, the distinct discrepancy in chemical characteristics between these Entrada (red rectangle) and Navajo (brown rectangles) aquifers is presumably due to the segregation of 40-70 m thick low-permeability Carmel formation.

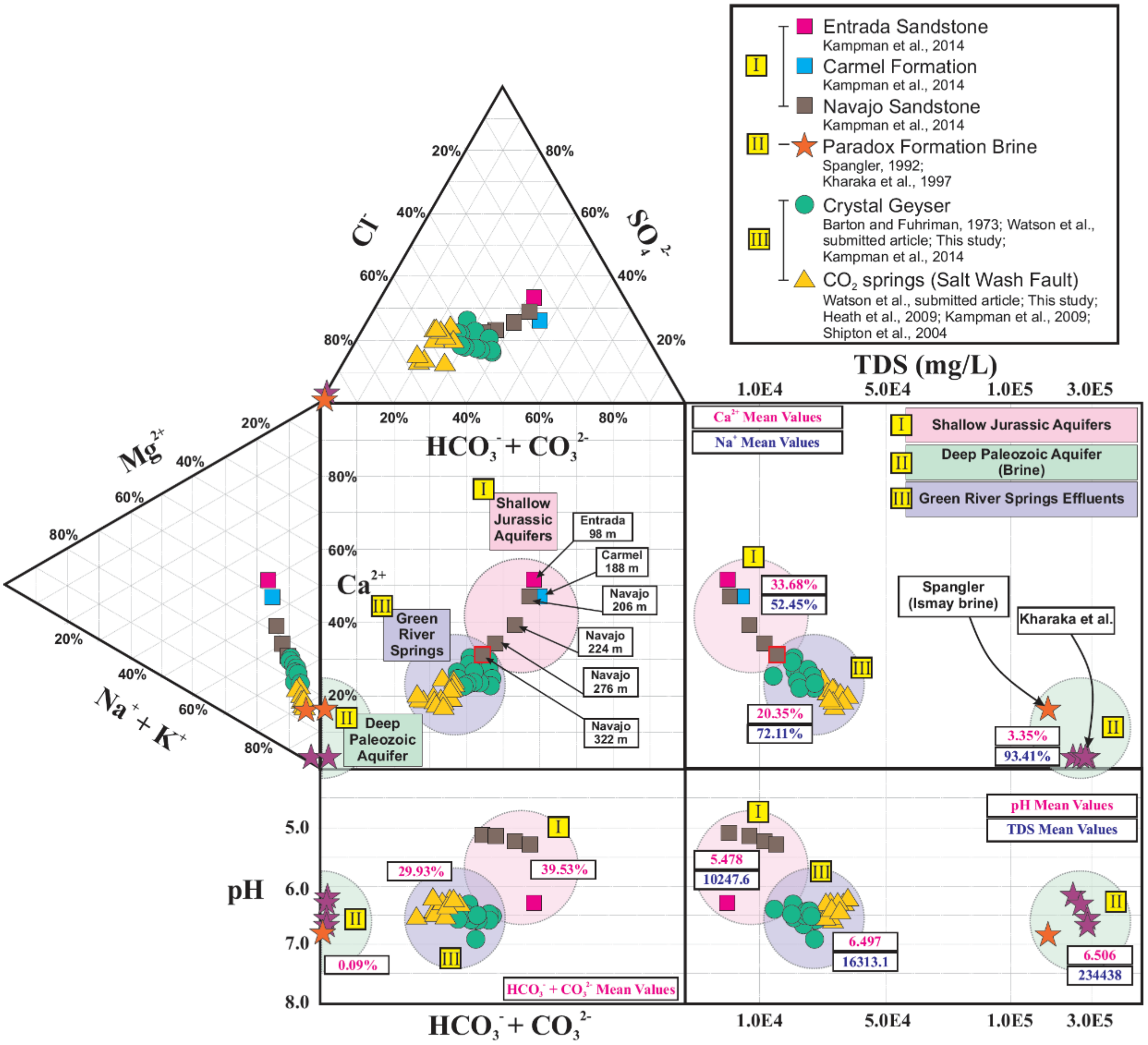

Figure 4. A modified Durov diagram plotting samples from the shallow Jurassic aquifers (Entrada, Camel, and Navajo formations), deep Paleozoic aquifer, and the Green River springs (geysers and springs). Water chemistry data were collated from Kampman et al. (2014), Kampman et al. (2009), Heath et al. (2009), Shipton et al. (2004), Barton and Fuhriman (1973), Spangler (1992), Kharaka et al. (1997), Watson et al., (submitted article), and this study.

Group II (green) depicts the chemistry of Deep Paleozoic Aquifer, which was estimated from 5 samples gathered at adjacent hydrocarbon fields (Kharaka et al., 1997; Spangler, 1992). All these brine samples showed approximately 234,000 mg/L of TDS with highly Na^+-Cl^- rich compositions (Na^+: 93.4% and Cl^-: 97.4%) and pH of 6.51 (Fig. 4). In detail, the elevated concentrations of this deeply originated brine range at Ca^{2+}: 31.4 to 192.1 mmol/l, K^+: 28.1 to 114.3 mmol/l, Mg^{2+}: 60.9 to 310.0 mmol/l, Na^+: 2,263.0 to 5,024.0 mmol/l, Cl^-: 3,103.0 to 5,808.0 mmol/l, and SO_4^{2-}: 2.1 to 61.8 mmol/l (Table 3).

Group III (purple) represents the effluents of the Green River Springs on both the LGW and SW fault traces, reflecting a mixing between Groups I and II (Fig. 4); major cation/anion concentrations, pH, and TDS of Group III lie in between Group I and II within all planes of the Durov diagram (Fig. 4). Means of HCO_3^-+CO_3^{2-}, Ca^{2+}, Na^+, pH, and TDS throughout Group III were 29.9%, 20.4%, 72.1%, 6.5 and 16,313.0 mg/L, respectively. Considering the semi-log plane (Ca^{2+} vs. log TDS), the concentration of Group II is one-order greater than the other groups, and Group I and Group III are clustered together. These data infer that the Green River Springs effluents are apparently fed by the Shallow Jurassic Aquifers due to their close proximity of chemistry. Similarly, Heath (2004) and Kampman et al. (2014) supported this observation from analyses of $\delta^{18}O$ and δD isotopes in the Green River Springs effluents and revealed that approximately 80-90% of the Green River Springs effluents originated from the Shallow Jurassic aquifers, and the remaining 10-20% from the Deep Paleozoic Aquifer.

Table 4. Chemistry of shallow Jurassic aquifer and Paleozoic brine. Drilling samples representing the shallow Jurassic aquifer (Entrada, Carmel, and Navajo) are from Kampman et al. (2014). Samples of the deep Paleozoic brine were from 1) Spangler (1992) and 2) Kharaka et al. (1997). *pH of the Entrada and Carmel formations were measured on the surface of the drilling site. **Indicates each different Paradox Valley Well brine source from Kharaka et al. (1997). ND stands for no measured data.

	depth	Temperature	pH	Ca^{2+}	Fe^{2+}	Sr^{2+}	K^+	Mg^{2+}	Na^+	Cl^-	SO_4^{2-}	Alkalinity	TDS
Formation	(m)	ºC	(in situ)	mmol/l	µmol/l	µmol/l	mmol/l	mmol/l	mmol/l	mmol/l	mmol/l	mEq/L	mg/L
Entrada	98	13.6	6.3*	27.64	348.93	186.30	3.25	10.75	47.65	26.84	17.86	45.00	7647
Carmel	188	15.5	6.2*	24.06	126.77	110.10	4.83	9.54	48.32	32.49	16.08	56.68	8711
Navajo	206	15.9	5.3	25.31	26.95	119.70	5.17	10.54	52.58	33.60	16.57	50.62	7788
Navajo	224	16.3	5.21	23.37	23.80	123.90	5.95	10.13	72.37	49.97	18.56	59.24	9339
Navajo	276	17.4	5.15	23.42	15.34	128.50	6.63	9.99	92.55	69.40	19.64	62.14	10730.6
Navajo	322	18.3	5.13	24.12	36.65	135.10	7.19	10.08	112.53	84.94	20.67	63.74	11967.7
Brine 1)	ND	24	6.8	192.1	ND	ND	28.14	65.84	2263	3103	11.45	1.23	173609
Brine 2)	2E**	ND	6.32	34.68	ND	ND	107.4	60.91	3990	4231	61.84	5.13	255038
Brine 2)	12E**	ND	6.56	33.18	ND	ND	114.3	62.55	3912	4147	61.63	4.23	250449
Brine 2)	4E**	ND	6.18	34.43	ND	ND	107.4	61.73	3851	4174	61.63	4.83	249789
Brine 2)	10E**	ND	6.67	31.44	ND	ND	109.2	64.2	3703	4090	61	3.7	243303

4. Reactive Transport Modeling Framework and Approaches

4.1. Numerical Simulation Methods

The multi-phase and multi-component reactive transport simulator, TOUGHREACT (Xu et al., 2004; Xu et al., 2006) was utilized to predict changes in reactive fluid chemistry and mineral assemblages when both the separate and dissolved phases of CO_2 migrate through the subsurface (Xu et al., 2004). The fluid properties of both CO_2/brine and their mixture are predicted with the ECO2N module, which covers the thermodynamic condition of 10 °C $\leq$ T $\leq$ 110 °C and P $\leq$ 600 bar (Spycher et al., 2003). Furthermore, the fugacity coefficient of $CO_{2(g)}$ follows Spycher and Reed (1988) and activity coefficients of aqueous species are calculated by the extended Debye-Hückel equation (Helgeson et al., 1981). Equilibrium constants for minerals, aqueous and gaseous species are mainly sourced from the EQ3/6 database version 7.2b (Wolery, 1992), and minor revisions on thermodynamic properties of minerals and aqueous species have been incorporated from Xu et al. (2005). Precipitation and dissolution of minerals are dependent on the status of local equilibrium and/or kinetic conditions (Steefel and Lasaga, 1994). The kinetic laws are derived from the transition state theory (Lasaga, 1984) under control of the concentration of hydrogen and hydroxide ions, and dependent on acid-basis reactions, as shown below:

$$r_n = \left[k_{25}^{ne} exp\left[\frac{-E_a^{ne}}{R}\left(\frac{1}{T}-\frac{1}{298.15}\right)\right] + k_{25}^{H^+} exp\left[\frac{-E_a^{H^+}}{R}\left(\frac{1}{T}-\frac{1}{298.15}\right)\right] \cdot a_{H^+}^{n_{H^+}} + k_{25}^{OH^-} exp\left[\frac{-E_a^{OH^-}}{R}\left(\frac{1}{T}-\frac{1}{298.15}\right)\right] a_{OH^-}^{n_{OH^-}}\right] \cdot A_n\left|1-\Omega_n^{\theta}\right|^{\eta} \tag{1}$$

where the superscripts ^{ne}, $^{H+}$, and $^{OH-}$ are neutral, acid, and base mechanisms, respectively, and η and θ are experimental coefficients. The '*a*' is the activity of the species. Ω_n is the kinetic mineral saturation ratio of the equilibrium mineral index ‘n’, and k_{25} is the rate constant at 25 °C (298.15 °K). The terms r_n, Ea, R, and T stand for the reaction rate of mineral index ‘n’, the activation energy, the gas constant, and the absolute temperature in Kelvin, respectively. The values of parameters defined in the equation (1) have been collated for various minerals in Palandri and Kharaka (2004) (Table 8). Finally, permeability and porosity changes in fault conduit are calculated by the Kozeny-Carman relationship (Bear, 1972). Further description of the transition state theory is described in Appendix A, and reactions of minerals and aqueous species are described in Appendix B.

Table 5. Boundary conditions and initial grid compositions of 1-D and 2-D models. Regional geothermal gradient data were collated from Heath et al. (2009) and Smouse (1993). Top and bottom boundary conditions of temperature and pressure slightly varied by the values of vertical discretization (Δz). Rock density and heat capacity values were referred and modified from averaged data of Manger (1963) and Somerton (1992).

Model	Properties and Conditions	Assigned Values
1-D model	Number of elements: Size of each element (m): Rock density (kg m^{-3}): Rock heat capacity (kJ kg^{-1} $^{o}C^{-1}$):	x-direction: 1; y-direction: 1; z-direction: 120 Δx = 10; Δy = 1; Δz = 5 2,600 1,000
	Boundary conditions	• Top: Dirichlet-type constant pressure (0.12 MPa) and temperature (25.0 °C) • Bottom: Dirichlet-type constant pressure (5.86 MPa) and temperature (37.7 °C)
2-D model	Number of elements: Size of each element (m): Rock density (kg m^{-3}): Rock heat capacity (kJ kg^{-1} $^{o}C^{-1}$):	x-direction: 101; y-direction: 1; z-direction: 60 Δx = 300, 200, 100, 50, 25, 10, 5, 1; Δy = 1; Δz = 10 2,600 1,000
	Boundary conditions	• Top: Dirichlet-type constant pressure (0.14 MPa) and temperature (25.1 °C) • Lateral: Dirichlet-type hydrostatic pressure/temperature (25.1 to 37.7 °C) with 0.25 MPa elevated at the northern Navajo Sandstone grid-blocks • Bottom: Neumann-type no-flow with pressure of 5.86 MPa and temperature of 37.7 °C

4.2. Conceptual Models Describing Fault-Focused Flow in the LGW Fault

To evaluate changes in the LGW fault system resulting from the fault-focused flow, both 1- and 2-dimensional models were developed in this study (Fig. 5). The simplified 1-D model was developed to investigate the detailed water-rock interaction by implementing the upscaled LGW fault conduit configuration (Fig. 5a). A more complex 2-D model was built to assess reasonable subsurface CO_2 distribution by implementing fault structure (dip, throw, fault gouge, and damage zone) and the regional dip of stratigraphy (Fig. 5b and 5c).

The 1-D model consists of 120 grid-blocks with the discretization of $\Delta z = 5$ m, while the lateral width is fixed with $\Delta x = 10$ m and $\Delta y = 1$ m (Table 4). The model was vertically extended to the depth of 600 m from the surface to the Chinle Formation, covering the footwall-side stratigraphy of the LGW fault (Fig. 5a). For the initial condition, a hydrostatic pressure profile was assigned, and a temperature profile was applied based on a regional geothermal gradient of 21.2 °C/km with 25 °C at the top boundary (Heath et al., 2009; Smouse, 1993). With this given condition of CO_2 being set under the critical point (P = 7.38 MPa and T = 31.1°C), CO_2 stayed in a gas phase throughout the model. Vertical permeability of 1.0×10^{-15} m^2 was uniformly assigned with a porosity of 0.2 (Table 5), based on setting the LGW fault as the low-permeability fault ($10^{-17} < k_h < 10^{-16}$ m^2 and $5\times10^{-16} < k_v < 10^{-15}$ m^2). The assigned k values were quantified in Jung et al. (2015) after the calibration of the model with the field-monitored spatial CO_2 flux dataset. Salt mass fraction ($X_{sm} = 0.011$) was calculated from the Crystal Geyser effluent, which was uniformly assigned in the model. Relative permeability and capillary pressure functions for $CO_{2(g)}$ and brine were predicted from the van Genuchten-Mualem model and the van Genuchten model, respectively (Table 6) (Corey, 1954; van Genuchten, 1980). For the boundary conditions, the Dirichlet condition was assigned at both the top and bottom grid-blocks (Table 4).

Table 6. Porosity (φ) and permeability (k) of each geologic formation in the study area. Stratigraphy data were collated from Allis et al. (2001), Burnside (2010), Hansley (1995), Hood and Patterson (1984), White et al. (2004), Zuluaga et al. (2014), and Jung et al. (2015). k_h and k_v are horizontal and vertical permeability of each formation, respectively. Upscaled vertical permeability value of 1-D simulation and modeled fault conduit parameters follow the estimated low-k fault values of Jung et al. (2015).

	Units (age)	Formation	Porosity (φ)	k_h (m^2)	k_v (m^2)
1-D	Upscaled	Fault Conduit	0.2	1.0×10^{-16}	1.0×10^{-15}
2-D	Units (age)	Formation	Porosity (φ)	k_h (m^2)	k_v (m^2)
	CRETACEOUS	Cedar Mountain Formation	0.10	1.0×10^{-15}	1.0×10^{-16}
	JURASSIC	Morrison Formation	0.20	1.0×10^{-15}	1.0×10^{-16}
		Summerville Formation	0.10	1.0×10^{-17}	1.0×10^{-18}
		Entrada Sandstone	0.30	1.0×10^{-13}	1.0×10^{-14}
		Carmel Formation	0.20	1.0×10^{-17}	1.0×10^{-18}
		Navajo Sandstone	0.20	5.3×10^{-13}	5.3×10^{-14}
		Kayenta Formation	0.20	1.0×10^{-15}	1.0×10^{-16}
		Wingate Sandstone	0.20	3.6×10^{-13}	3.6×10^{-14}
	TRIASSIC	Chinle Formation	0.05	2.0×10^{-17}	2.0×10^{-18}
		Moenkopi Formation	0.05	2.0×10^{-17}	2.0×10^{-18}
	Fault Conduit	Fault Plane	0.30	1.0×10^{-18}	1.0×10^{-17}
		Damage Zone	0.15	1.0×10^{-16}	1.0×10^{-15}
		Fault Gouge	0.21	2.2×10^{-13}	2.2×10^{-14}

$CO_{2(g)}$ with 60% saturation ($S_{CO2} = 0.6$) was then released at the bottom boundary to mimic the influx of CO_2 from the Deep Paleozoic Aquifer. The intensity of the CO_2 source representing $S_{CO2} = 0.6$ was adapted from Jung et al. (2015), who identified subsurface CO_2 distribution and accumulation within regional geometry of formations without consideration of chemical reactions. Finally, the model was simulated to predict the migration rate of the $CO_{2(g)}$ front and associated chemical reactions for a period of 300 yrs.

Table 7. Physical parameters for salinity, relative permeability and capillary pressure functions applied in both 1-D and 2-D model. References from $^{a)}$ Jung et al. (2015), $^{b)}$ Van Genuchten (1980), $^{c)}$ Corey (1954).

<table>
<tr><td colspan="2">Salinity (Salt Mass Fraction, X_{sm})</td><td>$0.011^{a)}$</td></tr>
<tr><td colspan="3">Relative Permeability</td></tr>
<tr><td>Phase</td><td>Liquid$^{b)}$ (S_{lr}: irreducible water saturation, λ: exponent)</td><td>Gas$^{c)}$ (S_{lr}: irreducible gas saturation)</td></tr>
<tr><td>Functions</td><td>$k_{rl} = \sqrt{S^*}\left\{1-\left(1-\left[S^*\right]^{1/\lambda}\right)^{\lambda}\right\}^2$
$S^* = \frac{S_l - S_{lr}}{1 - S_{lr}}$</td><td>$k_{rg} = \left(1-\overline{S}\right)^2\left(1-\overline{S}^2\right)$
$\overline{S} = \frac{S_l - S_{lr}}{1 - S_{lr} - S_{gr}}$</td></tr>
<tr><td>Parameters</td><td>$S_{lr} = 0.2$
$\lambda = 0.457$</td><td>$S_{gr} = 0.05$</td></tr>
<tr><td colspan="3">Capillary Pressure$^{b)}$ (S_{lr}: irreducible water saturation, m: exponent, P_0: strength coefficient)</td></tr>
<tr><td colspan="2">Functions</td><td>Parameters</td></tr>
<tr><td colspan="2">$P_{cap} = -P_0\left(\left[S^*\right]^{-1/\lambda} - 1\right)^{1-\lambda}$
$S^* = \frac{S_l - S_{lr}}{1 - S_{lr}}$</td><td>$S_{lr} = 0.00$
$\lambda = 0.457$
P_0 = 19.59 kPa</td></tr>
</table>

The 2-D model represents subsurface stratigraphy at the N-S cross-section of the Green River area, which intersects both the LGW fault and the Green River Anticline (Fig. 1b and 5b). The lateral extent of the 2-D model was set to 10,000 m while the depth of the model remained the same as the 1-D model. The horizontal discretization of the grid-block (Δx) varied from 300 m to 1 m in order to capture CO_2 transport and associated chemical reactions precisely adjacent to the LGW fault, and also for minimizing the lateral boundary effects of the model (Fig. 5b). Vertical discretization (Δz) was consistently set to 10 m, resulting in the total number of grid-blocks to be 6,060. Regional characteristics (e.g., dipping angle, thickness, and vertical offset) of all 13 geologic formations including the LGW fault were considered in the model, and the actual settings followed the former study of Jung et al. (2015) (Table 5). Configuration of the LGW fault conduit followed constituents (e.g., fault conduit, gouge, and damage zone) defined by Caine (1996), as shown in Fig. 5c. Here, geologic properties of fault plane and damage zone were adapted from Jung et al. (2015). The fault gouge surrounded by the damage zone was assigned with adjacent parent rock values, assuming that the fault gouge mainly originates from both cataclasites of parent rocks and clay-rich gouge, regardless of authigenic minerals in the damage zone (Caine, 1996; Faulkner et al., 2010); e.g., permeability of fault gouge material adjacent to the Navajo Sandstone was assigned a value identical to the Navajo Sandstone permeability. In addition, salinity, relative permeability, and capillary pressure were set to the same conditions as the 1-D models.

For the top boundary, the Dirichlet condition was assigned to represent atmospheric pressure and surface temperature (P = 0.14 MPa and T = 25.1 °C) while the no-flow condition (Neumann-type boundary) was given at the bottom boundary, precluding additional flow from underneath and highlighting the fault-focused fluid flow (Fig. 5b). Lateral boundaries of the model were set to maintain the initial hydrostatic pressure and geothermal gradient during the simulation period. Exceptionally, pressure of left-lateral boundary representing Navajo and Entrada Sandstones was increased 0.25 MPa from the hydrostatic pressure to reflect the over-pressurized aquifer condition as described in Kampman et al. (2014). For the sources, CO_2 was released at two designated locations (Fig. 5b): 1) CO_2 mass fraction (X_{CO2}) of 0.05 was assigned at the northern Navajo Sandstone boundary (leftmost boundary on the footwall side) to mimic natural CO_2 accumulations in the Shallow Jurassic Aquifers and 2) $CO_{2(g)}$ was assigned at the bottom of the LGW fault conduit, where 60% of CO_2 saturation ($S_{CO2} = 0.6$) was assigned equally to the 1-D model. Lastly, the simulation period was set to 1,000 yrs (Fig. 5b).

The hydrostatic pressure gradient applied to each model was implemented from theoretical CO_2 saturation calculations from in-situ observation of shut-in pressures at the CO_2W55 well by Kampman et al. (2014), and from former model settings of Jung et al. (2015). Slightly over-pressurized Carboniferous and Permian strata (i.e., high hydraulic heads), which forces groundwater toward the fault, are reflected on the model in the form of increased boundary pressure on the footwall side (Kampman et al. 2014; Hood and Patterson, 1984).

Sensitivity analyses on hydrogeologic model parameters were conducted prior to the actual modeling of the 1-D and 2-D systems in order to evaluate the influence of input variables on simulation results. Porosity, permeability and dilation width (Δx of fault zone grid-block) of the fault zone were varied during the analyses. First, since the applied porosity values in the study area were relatively higher (0.2 to 0.3) compared to the average Jurassic Sandstones (0.034 to 0.25; Manger, 1963), porosity values were varied by a factor of 2 during this test. Gain in porosity and permeability caused an increased speed of CO_2 fronts in the 1-D and 2-D models, and loss in porosity and permeability led to a decrease in migration velocity. For instance, when the porosity of 1-D and 2-D models was halved, the arrival time of CO_2 on the surface was approximately 15% slower than the original model. When the porosity was doubled, the migration velocity of CO_2 increased up to 20%. Furthermore, when the permeability of each model was halved, the arrival time of CO_2 on the surface was delayed about 40% of the original model. The dependency of flow velocity on the horizontal grid-block size (Δx) was not significant, showing ±5 % of difference when Δx varied up to one order of magnitude.

However, varying hydrogeologic parameters did not affect the distribution of CO_2 and mineral reaction patterns in the 1-D and 2-D models, but only the migration time of CO_2. Thus, the models and physical parameters in this study were set to match the CO_2 propagation rate of Jung et al. (2015) by using formerly suggested field values, to get a similar arrival time of CO_2 on the surface of the model, as displayed in Tables 5 and 6.

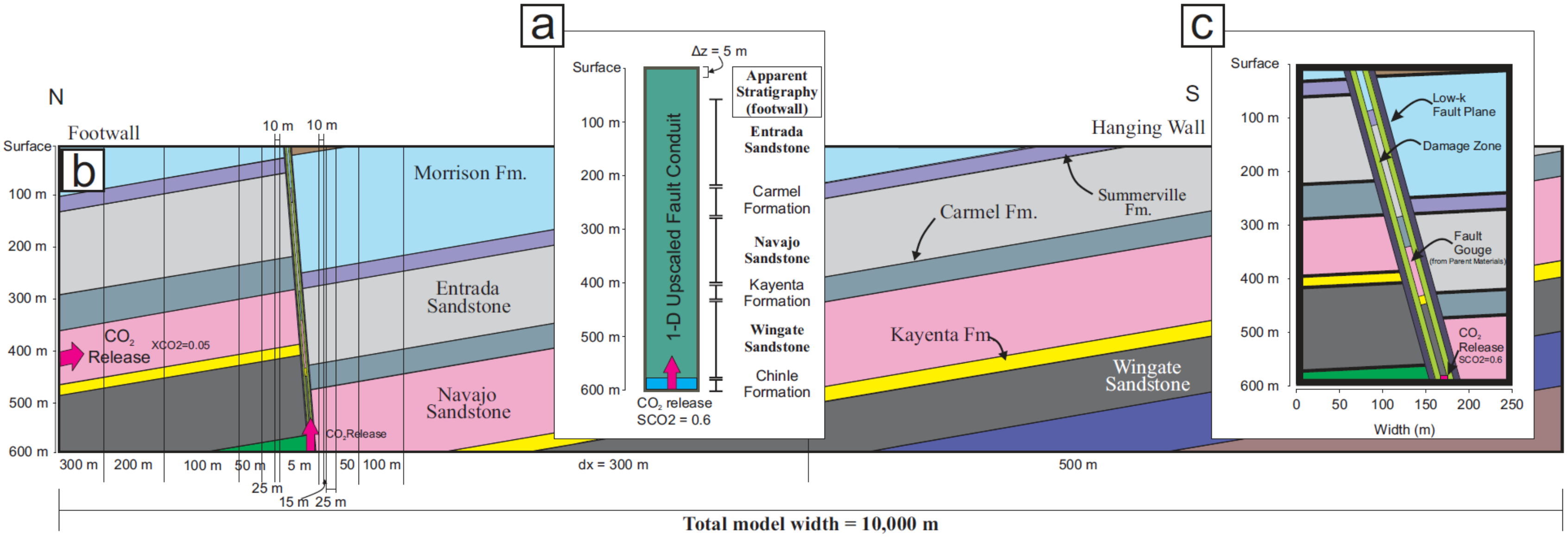

Figure 5. Conceptual models describing the Little Grand Wash Fault zone with fault-focused fluid flow; (a) a 1-D upscaled fault conduit model for investigation on mineralogic changes induced by CO_2 displacement. The apparent stratigraphy is estimated from stratigraphic information in the footwall side of the LGW fault. b) An overview of the 2-D conceptual fault zone model. CO_2 is released at two locations; gaseous CO_2 at the bottom of the LGW fault equivalent to the 1-D conduit model and aqueous CO_2 at the Navajo Sandstone in the lateral boundary of footwall. c) A magnified view of 2-D fault conduit shown in (b). Vertical solid lines in black represent changing grid-block sizes at the location.

4.3. Mineral Assemblage and Kinetic Parameters

The X-ray diffraction (XRD) analysis of the in-situ Navajo Sandstone core collected from CO_2W55 well revealed a quartz-rich lithology (Kampman et al., 2014) with ranges of quartz (80.4 to 93.0 wt.%), albite (0.0 to 0.4 wt.%), K-feldspar (2.5 to 8.7 wt. %), illite (1.5 to 8.4 wt. %), carbonate minerals as calcite and dolomite (0.4 to 4.8 wt. %), and hematite (0.0 to 0.1 wt. %). Additionally, the presence of kaolinite in the altered portion of the Navajo Sandstone (0.2 to 4.6 vol. %) was taken into account as a primary mineral species and applied in the models (Beitler et al., 2005). Based on these selected minerals, a series of numerical batch reactions was conducted with same 1-D and 2-D model settings of TOUGHREACT to identify an equilibrated initial fluid composition suitable to the local pressure and temperature gradients in the given media settings.

Following the outputs of batch reaction, the initial albite and dolomite facies were completely dissolved and transited to quartz, illite, calcite, and magnesite. Additionally, secondary pyrite was precipitated during this stage of modeling from a reaction with the ambient fluid. Consequently, 8 primary and 9 secondary mineral assemblages were selected (Table 7). Among the 8 primary minerals, calcite is assumed to be an equilibrium reaction according to the Ca^{2+}-rich condition of fluid chemistry in the research area. For the rest of the minerals, precipitation and dissolution were kinetically treated following the equation (1). Both rate constants and kinetic parameters are described in Table 7.

Initial volume fraction of minerals was converted from the weight fraction of the XRD dataset by assuming mineral grains to be a uniform and spherical radius (10^{-3} m). Mineral reactive surface area data were adapted from Xu et al. (2010) who calculated the areas by assuming the whole rock construction as a cubic array consisting of truncated spheres. For the clay minerals in this study, increased surface area of 151.6 cm^2/g was specifically applied to take into account surface edges within sheet silicates (Nagy, 1995). Reactive surface areas of the remaining minerals were comparable to values (near 10 cm^2/g) in Knauss et al. (2005) and Zerai et al. (2006). Finally, for the sake of numerical simplicity and due to limited data of crystalline composition, the chosen mineralogic data were uniformly applied to both 1-D and 2-D models with varying hydrogeologic parameters in each geologic formation (Table 5).

4.4. Chemical Species and Initial Aqueous Solutions

The modeled geochemical systems in this study are depicted by primary and secondary species, indicating basis species and aqueous complexes, respectively (Reed, 1982). In this case, the concentration of each secondary species is represented by a function of primary species (Reed, 1982), by the following equation:

$$C_i = K_i^{-1} \cdot \gamma_i^{-1} \cdot \prod_{j=1}^{N_j} C_j^{v_{ij}} \cdot \gamma_j^{v_{ij}} \qquad (2)$$

Here, C_i and C_j are the molal concentration of each i-th secondary and j-th primary species, respectively. γ_i and γ_j are activity coefficient of species. K_i and v^{ij} are the equilibrium constant of species i and the stoichiometric coefficient of reaction involving species ‘j’ in terms of ‘i’, respectively.

In this study, a total of 13 primary and 53 secondary species were selected based on speciation from the batch reaction with analytical fluid chemistry data (Table 8). Primarily, $O_{2(aq)}$ is used for representing the redox state of the ambient fluid in each grid-block in the models by attribution of the oxidation potential (Nordstrom and Munoz, 1986; Wolery, 1992, Xu et al., 2004). The negative $O_{2(aq)}$ concentration on Table 8 is assumed from Xu et al. (2004), which resulted from negative stoichiometric coefficient of aqueous oxygen in the deep saline water of models (Eh = -100 mV). This assumption corresponds to the field observation of Kampman et al. (2014), who reported the lower bound fluid Eh in the range of -100 to -150 mV.

In the 1-D model in Fig. 5a, the Crystal Geyser effluent was applied as the ambient fluid because the Crystal Geyser effluent is interpreted to be a mixture of the Deep Paleozoic and the Shallow Jurassic aquifers (Group I and II; Fig. 4). In the 2-D model, fluids of the two end-members, Entrada and Navajo Sandstones, were applied to each designated depth. For instance, the fluid chemistry of Entrada formation was applied to above the Carmel Formation at both the hanging wall and footwall. Consequently, the fluid chemistry in the Navajo formation was applied below the Entrada Sandstone (Fig. 5b). This 2-D model setting of differential fluids was established in order to simulate potential mixing of each end-member fluid on both aquifers and the fault zone.

5. Model Results

5.1. 1-D Fault Conduit Model

5.1.1. CO_2 displacement and Reactive Front Migration

Displacement of the ambient fluid within the 1-D LGW fault conduit occurred immediately after the release of $CO_{2(g)}$ began at the bottommost grid-block (Fig. 6a). $CO_{2(g)}$ saturation of 0.21 reached the middle of the Carmel Formation after 300 yrs (blue line in Fig. 6a). The migration velocity of $CO_{2(g)}$ through the 1-D fault conduit model similarly matched the former prediction by Jung et al. (2015), whose 2-D model predicted the arrival time of $CO_{2(g)}$ to the surface to be between 300 and 400 yrs. In the meantime, the migration velocity of $CO_{2(g)}$

continuously accelerated from 0.8 m/yr (~100 yrs; red line) and 1 m/yr (~200 yrs; green line) to 1.37 m/yr (~300 yrs; blue line) as the $CO_{2(g)}$ front approaches the shallower depths. Since CO_2 is compressible gas, which has lower density and viscosity compared to water, the migrating CO_2 front in the fault conduit will exert strong buoyancy force with accompanying volume expansion in the shallow depths (Pruess, 2007). In addition, an increase in CO_2 volume corresponds to a relative increase in its saturation within pores in the given medium, resulting in the enhancement of relative permeability of $CO_{2(g)}$ (Pruess, 2008).

Continued influx of $CO_{2(g)}$ at the bottom of the model gradually elevated the average CO_2 saturation within the fault conduit; as aforementioned, CO_2 saturation reached 0.21 at 300 yrs (Fig. 6a). Considering that the initial CO_2 saturation at the bottom was set to 0.6, it is implied that the remaining $CO_{2(g)}$ was dissolved into the ambient fluid. Hence, dissolved $CO_{2(aq)}$ concentration increased to 920 mmol/L at 300 yrs within the Navajo Sandstone (blue squares in Fig. 6a). In order for further quantification, the simulated $CO_{2(aq)}$ concentrations were compared with *in-situ* sampled CO_2 concentrations (yellow squares) collected at the CO_2W55 well, which was drilled 90 m north of the LGW fault trace (Kampman et al., 2014). Comparison of $CO_{2(aq)}$ generally revealed good agreement specifically at the bottom of the Navajo Formation despite that the well did not penetrate the LGW fault directly. Additionally, the basin-scale CO_2 solubility curve calculated from local pressure and temperature gradients using Duan et al. (2006) revealed similarity to the simulated CO_2 profile (Fig. 6a).

As a consequence of $CO_{2(g)}$ dissolution, acidification of the ambient fluid observed was coincident to the CO_2-moving front (Fig. 6b). For example, as $CO_{2(g)}$ migrated upward, pH of the ambient fluid declined to ~4.98 at 100 yrs (red), 5.13 at 200 yrs (green), and 5.17 at 300 yrs (blue). The migrating pH front was sharp early in both 100 yrs and 200 yrs, concurrently revealing the local pH minima at the front. However, the sharp low-pH fronts at 100 yrs and 200 yrs notably smoothed out at 300 yrs, resulting from buffering by water-rock interactions similar to an observation made by Xu et al. (2010). *In-situ* measured pH values (yellow squares) obtained at the lower part of Navajo Sandstone showed proximities to the simulated pH curve (blue line) at 300 yrs. However, field samples at the upper part of the Navajo Fm. have deviations of pH, which is similar to the profile of $CO_{2(aq)}$ concentration in Fig. 6a. This discrepancy occurred presumably due to the simplification of the 1-D model from adapting the uniform hydrogeological properties (e.g., permeability and porosity) throughout the model (Table 5).

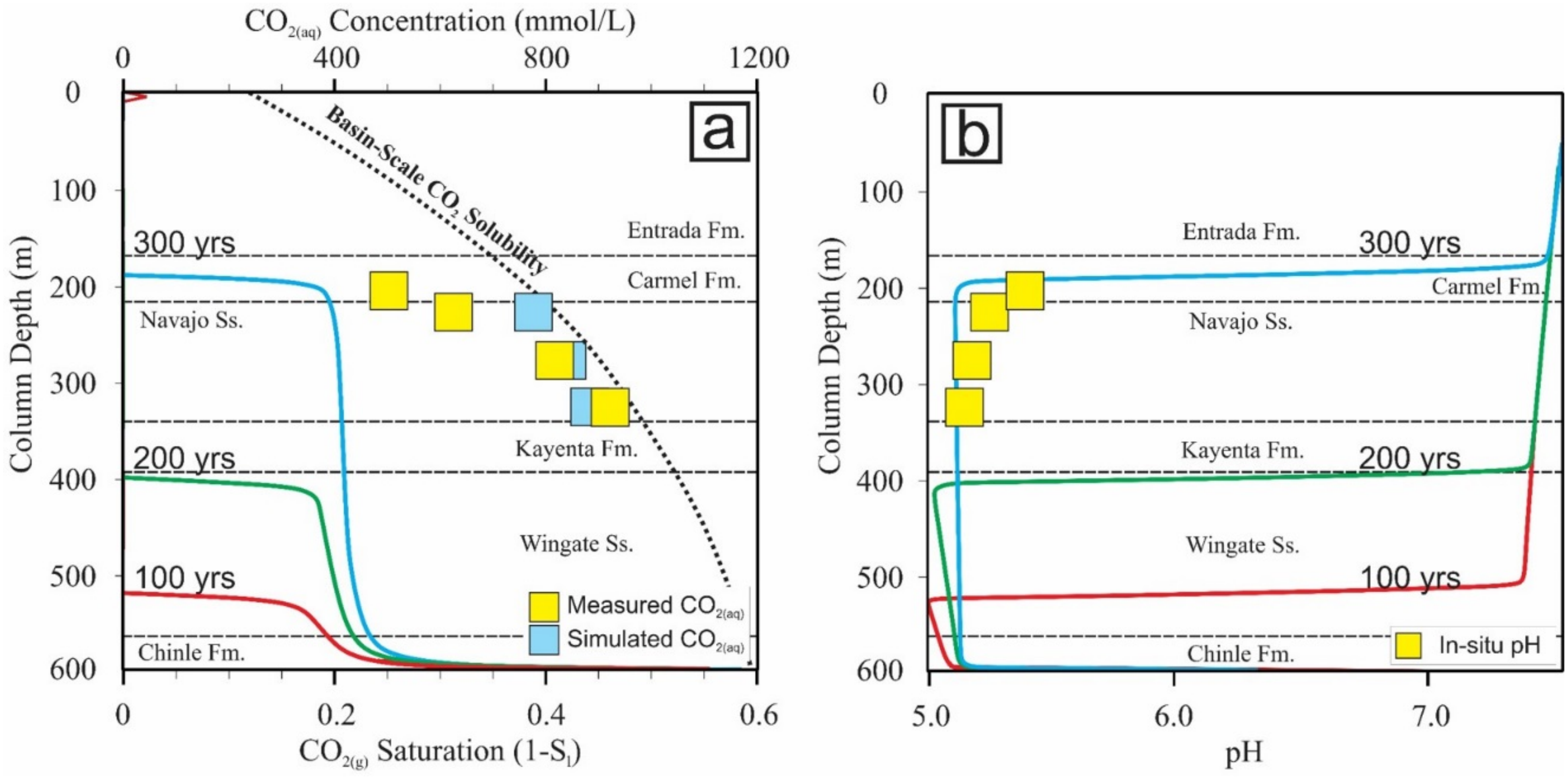

Figure 6. Results of 1-D simulation along the vertical column (depth=600m; Δz=5m; stratigraphy of the northern footwall is presented on Fig. 5) during 300 years of period. a) Calculated gas saturation and computed/measured $CO_{2(aq)}$ concentrations, where S_L represents saturation of liquid phase in each grid-block. $CO_{2(g)}$ saturation is calculated by 1-S_L. Basin-scale CO_2 solubility curve was adapted from Kampman et al. (2014); b) Computed and measured pH values. Each colored section of background reflects the depth and thickness of each formation at the northern footwall of the LGW fault. Square symbols represent in-situ measured values from the CO2W55 wellbore (Kampman et al., 2014) and numerically computed values from simulation at 300 years. Abbreviations of Fm. and Ss. in figures stand for formation and sandstone, respectively.

5.1.2. Changes in Minerals and Fluid Chemistry

Changes in mineral assemblages are shown as: i) dissolution of calcite, magnesite, hematite, and K-feldspar and ii) precipitation of pyrite, illite, and quartz (Fig. 7). The largest mineralogical alteration appeared in the carbonate minerals (up to -6.5 $mol/m^3 \cdot solid$; Fig. 7a) while the rest showed changes less than 0.4 $mol/m^3 \cdot solid$. Due to the dissolution of calcite ($CaCO_3$) and magnesite ($MgCO_3$), dissolved Ca^{2+} and Mg^{2+} concentrations were elevated, showing an increase of Ca^{2+} and Mg^{2+} up to 0.025 $mol/kg \cdot H_2O$ in the ambient fluid (Fig. 7a and 8a).

This observation implies that the carbonate minerals are the most sensitive to the dissolved CO_2, which induces an increase in dissolved inorganic carbons and lowers pH of the ambient fluid (Rau and Caldeira, 2000). Especially, the dissolution fronts of calcite were greater in the beginning but decreased as the CO_2 front moved upward, implying re-precipitation of calcite after dissolution (Fig. 7a). Therefore, the prolonged leakage of CO_2 could supply sufficient amounts of Ca^{2+} to the ambient fluid, resulting in a supersaturated condition with respect to calcite. On the contrary, magnesite did not reach the supersaturated condition, and thus, continuously dissolved with increasing Mg^{2+} concentration (Fig. 7a and 8a), indicating minimal precipitation of Mg-bearing minerals such as dolomite, illite, and ankerite.

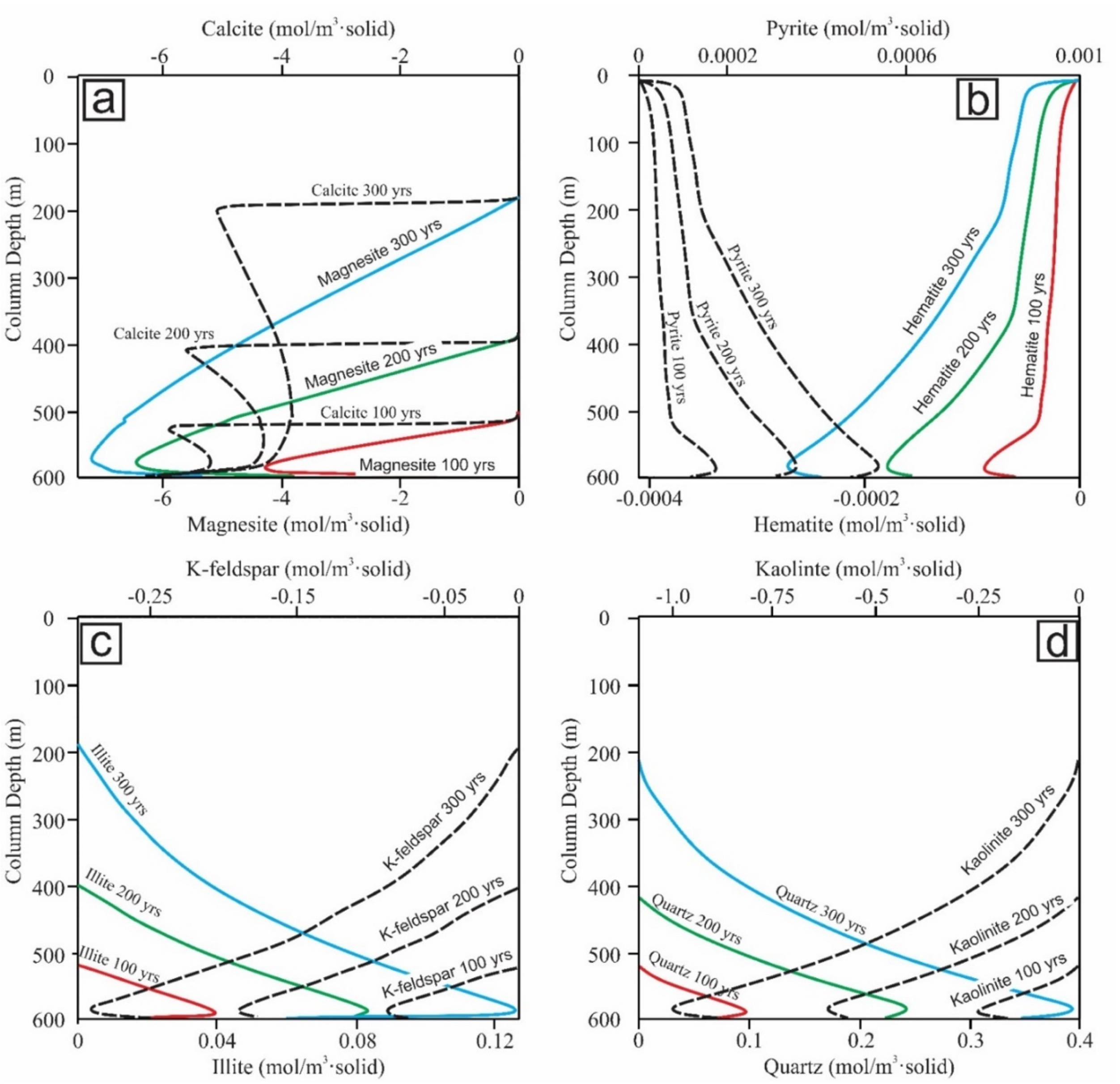

Figure 7. Changes in mineral assemblages of 1-D model. a) calcite and magnesite; ; b) pyrite and hematite c) K-feldspar and illite; d) quartz and kaolinite. Note that the unit of all mineral is changes in mol/m^3·solid in each individual grid-block. Note that each graph does not indicate an exchange between two minerals displayed therein.

The exchange of iron species between Fe-bearing minerals such as pyrite (FeS_2) and hematite (Fe_2O_3) is shown in Fig. 7b. As a consequence of continued CO_2 influx into the ambient fluid, the total dissolved amount of hematite reached ~0.00028 mol/m^3·solid at 300 yrs. In the meantime, the precipitated amount of pyrite (~0.00056 mol/m^3·solid) was approximately double that of the dissolved hematite. In the model, such pyrite precipitation and hematite dissolution are controlled by $O_{2(aq)}$ content in the ambient fluid (Xu et al., 2000). Although hematite actually contains Fe^{3+}, because the concentration of species is represented in the model in terms of total numerical concentration (Reed, 1982), the sum of aqueous Fe^{2+} and $O_{2(aq)}$ is calculated and utilized in the stead of Fe^{3+}. This oxygen approach to represent redox condition is described in Nordstrom and Munoz (1986) and Wolery (1992).

In the model, the dissolution of hematite releases Fe^{2+}, which is used in the following equations to calculate the precipitation of pyrite (Xu et al., 2000):

$$Fe_2O_3 + 4H^+ \leftrightarrow 2Fe^{2+} + 0.5O_2 + 2H_2O \qquad (3)$$

$$FeS_2 + H_2O + 3.5O_2 \leftrightarrow Fe^{2+} + 2H^+ + 2SO_4^{2-} \qquad (4)$$

These equations revealed that the precipitation of pyrite consumes the total amount of sulfate and proton within the ambient fluid (Fig. 8b). The source of Fe in the iron concretions including pyrite was indicated as the host-rock itself (e.g., dissolution of hematite), based on proton-promoted or reductive dissolution of iron-oxides in the rock, much like the dissolving hematite in the models of this study (Busigny and Dauphas, 2007). In addition, former studies indicated that the presence of small and disseminated pyrite grains in bleached sandstones show that Fe was mobilized and migrated in a form of Fe(II) (Beitler et al., 2005; Parry et al., 2004). In addition, these previous studies noted that a mixing between reducing fluid and groundwater may have induced the concretion of iron-bearing minerals in the region; this is reflected in model-observed pyrite-hematite reactions in this study (Chan et al., 2000).

Although the overall reaction of hematite-pyrite oxidizes the ambient fluid by releasing $O_{2(aq)}$, the initial reducing condition in the model is likely to cause these transitions of iron-bearing minerals. Thus, during a period of 300 yrs., average concentrations of redox aqueous species in the model varied by the influx of CO_2. An increase in HS^- and S^{2-} (8.49×10^{-3} mol/kg·H_2O and 1.24×10^{-8} mol/kg·H_2O) is caused by a sum of the reduced portion of H_2S, $SO_{2(aq)}$ and SO_4^{2-} (-6.85×10^{-3} mol/kg·H_2O, -2.39×10^{-19} mol/kg·H_2O and -6.12×10^{-8} mol/kg·H_2O) in each grid-block on average. Furthermore, small changes in hematite occurred above the CO_2 fronts without influence of CO_2 as a result of the reducing condition in the ambient fluid (pH = 6.52; Eh = -100 mV) that exceeds the stable range of hematite in the regional aquifer settings (Chan et al., 2000).

In addition, a minor increment of $CH_{4(aq)}$ in the medium was observed ($\sim 1.0 \times 10^{-3}$ mol/kg·H_2O), indicating a reinforced reducing condition established by the migration of CO_2-laden fluid in the model. As suggested by Wigley et al. (2012), who used a thermodynamic modeling method PHREEQC (Parkhurst and Appelo, 1999) with WATEQ4F database (Ball and Nordstrom, 1991), the overall stoichiometric dissolution of hematite in the region was stated as the following equation:

$$20Fe_2O_3 + 5CH_4 + 64CO_2 + 19H_2O + 11H^+ = 30Fe^{2+} + 10FeHCO_3^+ + 59HCO_3^- \quad (5)$$

Furthermore, the precipitation of pyrite and reduction of sulfur in this study is shown by the following equation (Parry et al., 2004):

$$4Fe_2O_3 + 16SO_4^{2-} + 17H^+ + 15CH_{4(g)} = 8FeS_2 + 31H_2O + 15HCO_3^- \quad (6)$$

As methane reacts with the ambient fluid, the redox potential of fluid decreases to sulfate reduction, which is necessary for pyrite precipitation (Parry et al., 2004); thus, sulfate in the fluid is reduced to S_2^{2-}. Therefore, a trace amount of CH_4 is needed to keep the redox state of the ambient fluid, but an increased activity of CH_4 is not necessary to promote further dissolution of hematite (Wigley et al., 2012). The presence of CH_4 in the region was previously reported by Wigley et al., (2012), indicating the aforementioned reductive fluid chemistry.

Fe^{2+} in the ambient fluid consistently increased, although the amount was almost negligible (Fig. 8d). Thus, it is implied that the dissolution rate of hematite slightly exceeds the precipitation rate of pyrite in the given condition of ambient fluid chemistry. In addition, because the change of $Fe^{2+}_{(aq)}$ is significantly small when compared to the range of molar changes that occurred in the two mineral abundances, this indicates the instantaneous and direct precipitation of iron into pyrite.

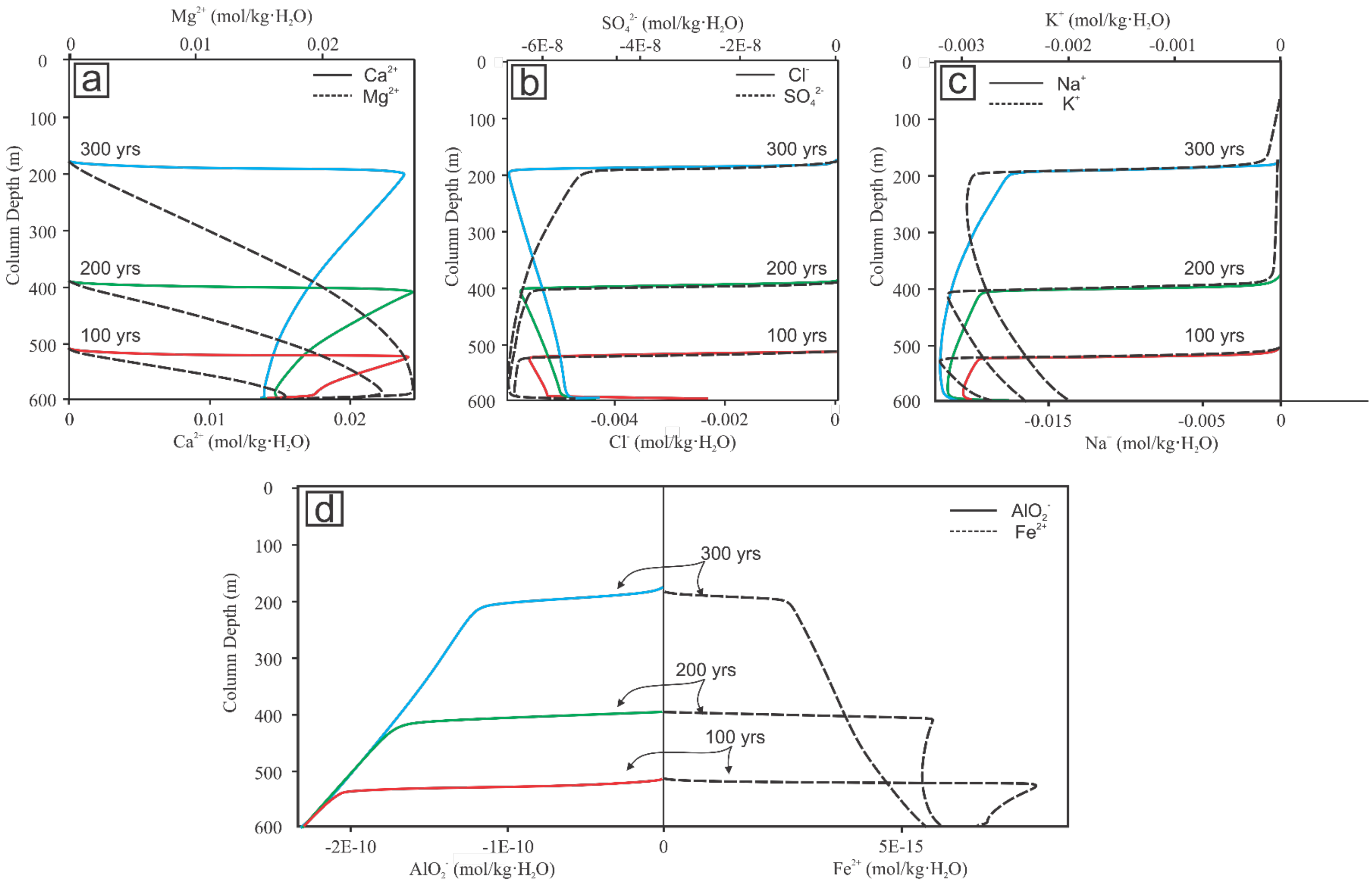

Figure 8. Changes in element concentrations of 1-D simulation along the vertical column during 300 years of simulation period. a) Ca^{2+} and Mg^{2+}; b) SO_4^{2-} and Cl^-; c) Na^+ and K^+; d) AlO_2^- and Fe^{2+}. Unit of all concentrations is changes in mol/kg·H_2O in each individual grid-block.

Table 8. Parameters for computing kinetic rate constants in the model (Eqn. 1-2 in Appendix A). The kinetic constants are collated from Golubev et al (2009), Holland and Powell (1998), Knauss et al. (2005), McKibben and Barnes (1986), Palandri and Kharaka (2004), Ruan and Gilkes (1995), Tester et al. (1994). Dolomite kinetic data were calculated by Xu et al. (2010), using Gibbs free energy values of Rock et al. (2001) and entropy works of Robie and Hemingway (1995). Where k_{25} = kinetic constant at the temperature of 25°C, Ea = activation energy. For equation 1 and 2, the power term ^{n} for acid and base mechanisms both are described with respect to H^+. Since the pyrite mechanisms are dependent of $O_{2(aq)}$, H^+ and Fe^{3+}, n of neutral mechanism is derived from O_2, and ^{n} for acid mechanism is with respect to H^+ and Fe^{3+}. Calcite was applied as an equilibrium reaction species, and the initial volumetric fraction as zero. a) Initial volume fraction of each mineral was based on XRD analyses on the Navajo Sandstone of Kampman et al. (2014).

Mineral	**Chemical Composition**	**Initial Volume Fraction**$^{a)}$	**Specific Surface Area** (cm^2/g)	**References**
Primary				
Quartz	SiO_2	9.55×10^{-1}	9.8	Tester et al. (1994)
Hematite	Fe_2O_3	4.39×10^{-4}	12.9	Ruan and Gilkes (1995)
Illite	$K_{0.6}Mg_{0.25}Al_{1.8}(Al_{0.5}Si_{3.5}O_{10})(OH)_2$	1.51×10^{-2}	151.6	set to smectites
K-feldspar	$KAlSi_3O_8$	1.02×10^{-2}	9.8	Palandri and Kharaka (2004)
Kaolinite	$Al_2Si_2O_5(OH)_4$	1.86×10^{-2}	151.6	Palandri and Kharaka (2004)
Magnesite	$MgCO_3$	2.49×10^{-4}	9.8	Palandri and Kharaka (2004)
Pyrite	FeS_2	9.48×10^{-8}	12.9	McKibben and Barnes (1986)
Calcite	$CaCO_3$	3.94×10^{-4}		
Secondary				
Dolomite	$CaMg(CO_3)_2$	0	9.8	Xu et al. (2010)
Chlorite	$Mg_{2.5}Fe_{2.5}Al_2Si_3O_{10}(OH)_8$	0	9.8	Holland and Powell (1998)
Oligoclase	$CaNa_4Al_6Si_{14}O_{40}$	0	9.8	Palandri and Kharaka (2004)
Albite	$NaAlSi_3O_8$	0	9.8	Palandri and Kharaka (2004)
Siderite	$FeCO_3$	0	9.8	Knauss et al. (2005); Golubev et al (2009)
Dawsonite	$NaAlCO_3(OH)_2$	0	9.8	set to siderite
Ankerite	$CaMg_{0.3}Fe_{0.7}(CO_3)_2$	0	9.8	set to siderite
Na-Smectite	$Na_{0.290}Mg_{0.26}Al_{1.77}Si_{3.97}O_{10}(OH)_2$	0	151.6	Palandri and Kharaka (2004)
Ca-Smectite	$Ca_{0.145}Mg_{0.26}Al_{1.77}Si_{3.97}O_{10}(OH)$	0	151.6	Palandri and Kharaka (2004)

Table 8 (continued).

Mineral	Kinetic rate parameters							
	Neutral Mechanism		Acid Mechanism			Base Mechanism		
	k_{25} (mol/m^2/s)	Ea (kJ/mol)	k_{25} (mol/m^2/s)	Ea (kJ/mol)	n (H^+)	k_{25} (mol/m^2/s)	Ea (kJ/mol)	n (H^+)
Primary								
Quartz	1.02×10^{-14}	87.7						
Hematite	2.51×10^{-15}	66.2	4.07×10^{-1}	66.2	1.00			
Illite	1.66×10^{-13}	35.0	1.05×10^{-11}	23.6	0.34	3.02×10^{-17}	58.9	-0.40
K-feldspar	3.89×10^{-13}	38.0	8.71×10^{-11}	51.7	0.50	6.31×10^{-12}	94.1	-0.82
Kaolinite	6.92×10^{-14}	22.2	4.89×10^{-12}	65.9	0.78	8.91×10^{-18}	17.9	-0.47
Magnesite	4.57×10^{-10}	23.5	4.17×10^{-7}	14.4	1.00			
Pyrite	2.82×10^{-5} n($O_{2(aq)}$) = 0.5	56.9	3.02×10^{-8} n(Fe^{3+}) = 0.5	56.9	-0.50			
Calcite	Equilibrium reaction							
Secondary								
Dolomite	2.95×10^{-8}	52.2	6.46×10^{-4}	36.1	0.50			
Chlorite	3.02×10^{-13}	88.0	7.76×10^{-12}	88.0	0.50			
Oligoclase	1.45×10^{-12}	69.8	2.14×10^{-10}	65.0	0.46			
Albite	2.75×10^{-13}	69.8	6.92×10^{-11}	65.0	0.46	2.52×10^{-16}	71	-0.57
Siderite	1.26×10^{-9}	62.8	6.46×10^{-4}	36.1	0.50			
Dawsonite	1.26×10^{-9}	62.8	6.46×10^{-4}	36.1	0.50			
Ankerite	1.26×10^{-9}	62.8	6.46×10^{-4}	36.1	0.50			
Na-Smectite	1.66×10^{-13}	35.0	1.05×10^{-11}	23.6	0.34	3.02×10^{-17}	58.9	-0.40
Ca-Smectite	1.66×10^{-13}	35.0	1.05×10^{-11}	23.6	0.34	3.02×10^{-17}	58.9	-0.40

Table 9. Initial water chemistry of each reactive transport model. All models follow the same chemical species setting in this study. Fluid chemistry values were adapted from the averaged values of Table 3 and converted into model input format. a) All secondary species are described in terms of total concentration of primary species (Reed, 1982), where A_{TOT} stands for total numerical concentration of species "A". All initial water composition is equilibrated in the model for 2,000 yrs. b) Brine end-member was selected from well 2E fluid chemistry of Kharaka et al. (1997) as a representative value for the Deep Paleozoic Aquifer. $O_{2(aq)}$, H^+ and H_2O are assigned in the model to give fluid properties of redox balance, pH and initial solvent, respectively. $O_{2(aq)}$ values were assumed from Xu et al. (2006) who evaluated CO_2 behavior in deep sedimentary basins and uniformly applied on all cases to have same redox condition. (*Formation fluid samples from Kampman et al., 2014)

Primary Species (A_{TOT})$^{a)}$	Secondary Species (designated role on reactions)	Chemical Components (mmol/L)	Entrada*	Navajo*	Crystal Geyser
H^+	pH	pH	6.30E+00	5.13E+00	6.79E+00
Na^+	$NaCl_{(aq)}$, $NaCO_3^-$, $NaHCO_{3(aq)}$, $NaHSiO_{3(aq)}$, $NaOH_{(aq)}$, $NaSO_4^-$	Na^+	4.76E+01	1.13E+02	1.55E+02
K^+	$KCl_{(aq)}$, KSO_4^-	K^+	3.30E+00	7.20E+00	8.31E+00
Ca^{2+}	$CaCl^+$, $CaCl_{2(aq)}$, $CaCO_{3(aq)}$, $CaHCO_3^+$, $CaOH^+$, $CaSO_{4(aq)}$	Ca^{2+}	2.76E+01	2.41E+01	2.48E+01
Mg^{2+}	$MgHCO_3^+$, $MgCO_{3(aq)}$, $MgCl^+$, $MgH_3SiO_4^+$, $MgOH^+$, $MgSO_{4(aq)}$	Mg^{2+}	1.07E+01	1.01E+01	9.10E+00
Fe^{2+}	Fe^{3+}, $FeHCO_3^+$, $FeCO_{3(aq)}$, $FeCl^+$, $FeCl_4^{2-}$	Fe^{2+}	3.49E-01	3.66E-02	2.50E-04
AlO_2^-	Al^{3+}, $HAlO_{2(aq)}$, $NaAlO_{2(aq)}$, $AlOH^{2+}$, $Al(OH)_2^+$	AlO_2^-	3.00E-04	1.20E-03	5.50E-06
$SiO_{2(aq)}$	$H_3SiO_4^-$	$SiO_{2(aq)}$	1.06E-01	5.92E-02	2.46E-01
HCO_3^-	$CaCO_{3(aq)}$, $CaHCO_3^+$, $FeHCO_3^+$, $FeCO_{3(aq)}$, $MgHCO_3^+$, $MgCO_{3(aq)}$, $NaCO_3^-$, $NaHCO_{3(aq)}$, $CO_{2(aq)}$, CO_3^{2-}, $CH_{4(aq)}$, $CH_3COOH_{(aq)}$	HCO_3^-	4.50E+01	6.37E+01	7.11E+01
Cl^-	$CaCl^+$, $CaCl_{2(aq)}$, $FeCl^+$, $FeCl_4^{2-}$, $KCl_{(aq)}$, $MgCl^+$, $NaCl_{(aq)}$	Cl^-	2.68E+01	8.49E+01	3.70E+00
SO_4^{2-}	$H_2S_{(aq)}$, HS^-, S^{2-}	SO_4^{2-}	1.94E+01	2.35E+01	2.21E+01
$O_{2(aq)}$	Redox Balance	$O_{2(aq)}$	-8.65E-02	-8.65E-02	-8.65E-02
H_2O	Initial Solvent	**H_2O**	1.00E+00	1.00E+00	1.00E+00

Reactions of silicate minerals (K-feldspar, kaolinite, illite, and quartz) also corresponded to the migration of the reactive front (Fig. 7c and 7d). Continuous precipitation of illite and quartz, and dissolution of K-feldspar and kaolinite were observed; these changes were relatively less significant than carbonate minerals (~0.4 mol/m^3·solid) but greater than Fe-bearing species. However, SiO_2 and Fe_2O_3 concentrations showed an inverse correlation in a field study (Busigny and Dauphas, 2007).

A considerable amount of quartz precipitated along the fault conduit at the relatively lower temperature settings of the model (25 – 37.7 °C; Fig. 7c). Precipitation of quartz occurs in response to the lowered temperature and pressure when the saturated fluid migrates upward through the fault conduit (e.g., Sibson, 1990). In the model, illite precipitation caused consumption of the K^+ ion, which was released from K-feldspar and kaolinite dissolution as the reactive front moved upward (Fig. 7c and 8c). In addition, the Na^+ ion was consumed to form a secondary Na^+-species in the given pH condition, while no precipitation of Na-bearing minerals (i.e., oligoclase, dawsonite and Na-smectite) was observed (Fig. 8c; Table 7 to 8). On the contrary, the concentration of AlO_2^-, resulting from the precipitation of illite with a minor amount of aqueous complexation, continuously decreased in the model (Fig. 8d).

Due to model limitations, amorphous silica ($SiO_{2(am)}$) was not included in the model components; quartz and $SiO_{2(am)}$ compete with the same amount of $SiO_{2(aq)}$ in the model and thus, lead to the failure of model convergence. Hence, the model was not able to represent both the initial sandstone composition using quartz and the precipitation of $SiO_{2(am)}$ at the same time, due to numerical formulation of singular matrices. However, when $SiO_{2(am)}$ was solely assigned in the model instead of quartz, the precipitation pattern of the mineral was equivalent to the one of quartz. Therefore, in this study, quartz is used to represent the overall SiO_2 mineral precipitation.

Release of silica into the ambient fluid from the dissolution of these minerals mainly promotes the precipitation of quartz and illite in low temperatures by providing soluble silica for cementation of such minerals. Feldspar weathering and transition of smectite to illite were formerly suggested as the internal sources of silica precipitation in reservoir rocks; this is reflected in the model results (Weber and Ricken, 2005; Lynch et al., 1997). In addition, dissolution of feldspar in low-pH regions, forming an input of the SiO_2-rich ambient fluid, was formerly observed in the numerical model of the White Rim Sandstone on the Colorado Plateau with a reservoir temperature of 54 °C (White et al., 2005). At this temperature range, the $SiO_{2(aq)}$ concentration (~0.03 mol/kg·H_2O) in the ambient fluid, that is derived from a dissolution of kaolinite (~1 mol/m^3·solid) and feldspar (~0.25 mol/m^3·solid), overtakes the solubility of quartz by approximately 21 times (Morey et al., 1962).

5.2. 2-D Fault Zone Model

5.2.1. Distribution of Subsurface CO_2 in the 2-D Fault Zone Model

CO_2 distribution through the regional stratigraphic structures as shown in Fig. 5b is assessed in Fig. 9. Overall, CO_2 released from two designated sources (i.e., grid-blocks on the leftmost boundary at the Navajo Sandstone and the bottommost grid-blocks of fault conduit; Fig. 5b) that depicts CO_2 generated from the deep Paleozoic Aquifers and the natural CO_2-charged condition of the Navajo Sandstone (Jung et al., 2015), is spreaded through the LGW fault to the surface and accumulated under regional low-k caprocks (e.g., Summerville, Carmel, and Kayenta Formations; Fig. 9a; Table 5).

At the onset of the simulation, the buoyant CO_2 filled the bottom-most region within the LGW fault, and additional CO_2 supplied from the Navajo sandstone merged together at the LGW fault. Configuration of the LGW faults (i.e., fault conduit, gouge, and damage zone) governs CO_2 distribution as CO_2 migrated through the LGW fault. For example, throughout the 300-yr simulation period, CO_2 predominantly migrates through the high-k damage zone (Fig. 9b). When CO_2 became more saturated throughout the fault and encountered low-k gouges and planes, the CO_2 spread out and found other preferential pathways (Fig. 9c). Throughout the 2-D simulation, the vertical migration velocity of CO_2 within the LGW fault was estimated as 1.8 m/yr on average, which is slightly higher than the one predicted from the 1-D model (0.8-1.37 m/yr; Fig. 9d). This is because the 2-D model had two CO_2 sources assigned, resulting in a rapid supply of CO_2 specifically from the lateral Navajo Sandstone source (Fig. 9a).

The LGW fault is characterized as both the north-plunging anticlinal structure and low-k barrier that affect an accumulation of CO_2 under the subsurface (Jung et al., 2015). Hence, the anticlinal structure of the fault on the footwall side (the crest of anticlinal trap in Jung et al., 2015) showed strong CO_2 trapping ability than dipping formations in the hanging wall side. For instance, CO_2 saturations in Entrada, Navajo, and Wingate sandstones at the footwall side are more elevated than those of the handing wall side (Fig. 9d). Especially, in the footwall, the buoyant nature of CO_2 makes the plume remain stagnant at the crest of anticlinal structure where the low-k LGW fault intersects. Therefore, the small-scale CO_2 natural reservoir presumably built up in this location, and consequently, this accumulation of CO_2 could induce the geysering mechanisms at the Crystal Geyser (Fig. 9d). A certain amount of CO_2, which horizontally penetrates through the LGW fault, followed the regional Jurassic aquifers under the Summerville and Carmel Formations to the SW fault, implying that both LGW and SW faults are hydrodynamically connected each other and share the CO_2 origins (Fig. 9a). The estimated horizontal CO_2 migration velocity under regional dipping caprocks was 1.9 m/yr in average, which is compatible with the formerly predicted range of 2.2 to 2.4 m/yr by Jung et al. (2015). The estimated velocity suggested that the CO_2 plume will arrive at the SW Fault in approximately 4,200 yrs (Fig. 9a).

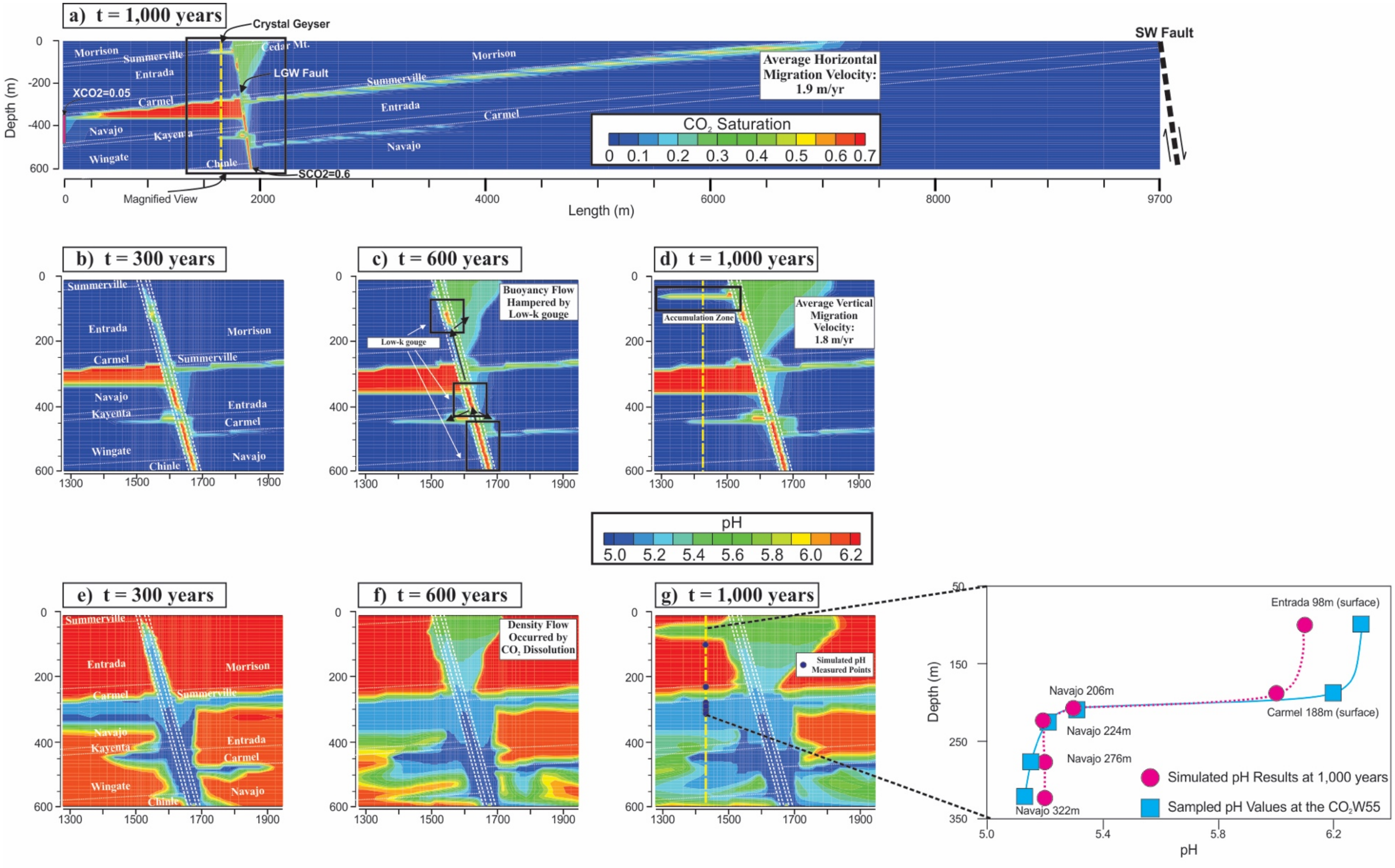

Figure 9. Two-dimensional CO_2 and pH distribution of the cross-sectional area depicted on Fig. 1b. a) Overall CO_2 saturation in 2-D model at 1,000 years of simulation period. Magnified view of CO_2 saturation along the fault zone at b) t = 300 years, c) t = 600 years and d) t = 1000 years. pH distribution along the fault zone at e) t = 300 years, f) t = 600 years and g) t = 1000 years with in-situ and modeled pH data along the Crystal Geyser. Note that pH values of the Entrada and Carmel Fm. were measured on the surface (Kampman et al., 2014).

Once CO_2 dissolved into the ambient brine, the density of CO_2-saturated brine increased 2 to 3 % greater than the ambient fluid, inducing a density-driven gravitational segregation (Garcia, 2001). Ultimately, convective mixing within formations occurred and further enhanced the CO_2 dissolution process. The pH changes shown in Fig. 9e, 9f and 9g are mainly driven by the gravitational segregation of dissolved CO_2. Especially, within the both Wingate and Navajo Formations, the gravitational segregation of dissolved CO_2 is significant, and thus, the low pH fluid is dominant. The pH observed at 1,000 yrs in Fig. 9 show overall range of 5.0 to 6.2 within the model but dropped to 5.0-5.4 specific to the fault zone (pH=5.1 on average of the 1-D model at 300 yrs; Fig. 6b). Furthermore, the simulated profile (yellow-dashed line) of pH along the Crystal Geyser shown in Fig. 9g approximately matched the *in-situ* sampled pH values at CO_2W55 well (Table 3).

5.2.2. Minerals and Fluid Changes in 2-D Subsurface Environment

Primary changes observed previously in the 1-D model were: 1) dissolution of carbonate minerals (calcite and magnesite); 2) an exchange of iron species between hematite and pyrite; 3) an alteration of silicate minerals (K-feldspar and kaolinite); and 4) an evolution of quartz/phyllosilicate facies. Focusing on these reactions, concentrations of major aqueous species and mineral abundances were tracked to understand the evolution of minerals and fluid chemistry in the 2-D model during a period of 1,000 yrs (Fig. 10 and Fig. 11). Patterns describing change in major aqueous species and minerals mimic the overall distribution of CO_2 plume (Fig. 9 and Fig. 10). As marked by the dashed lines (spatial extent of each element at 300 and 600 yrs) in Fig. 10, fronts of dissolved species corresponding to mineral dissolution regime

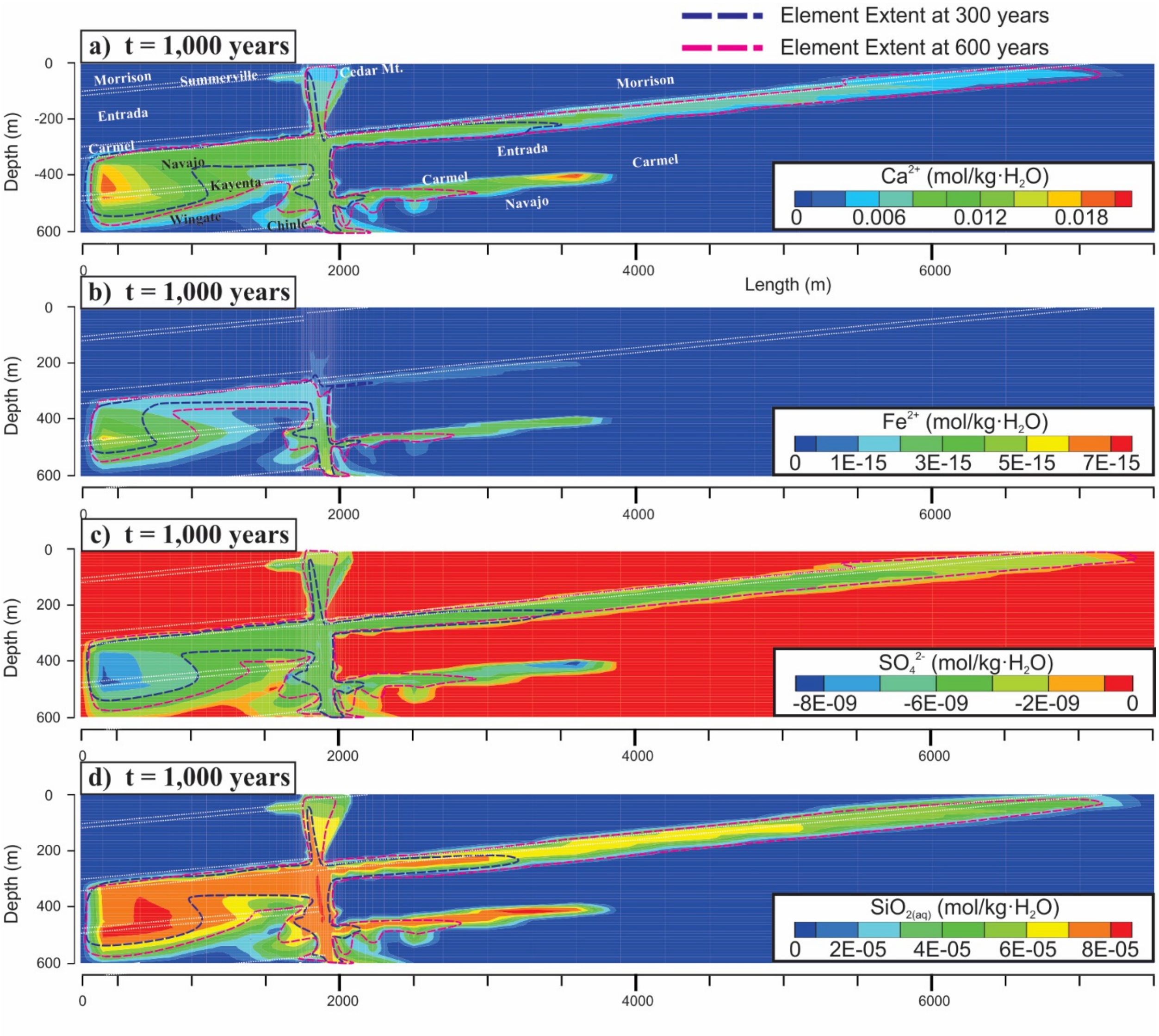

Figure 10. Two-dimensional distribution of the aqueous species and relevant mineral abundances at t = 1,000 years along the cross-sectional area depicted on Fig. 1b. Note that the right model boundary was cut at 7,500 m from the leftmost margin, to enhance visibility of figures. a) Ca^{2+} concentration; b) Fe^{2+} concentration; c) SO_4^{2-} concentration; f) pyrite abundance; d) $SiO_{2(aq)}$ concentration. The dashed lines with blue and magenta depicts the extent of each element species at 300 and 600 years, respectively. Note that SO_4^{2-} concentration values are negative, indicating consumption of the anion.

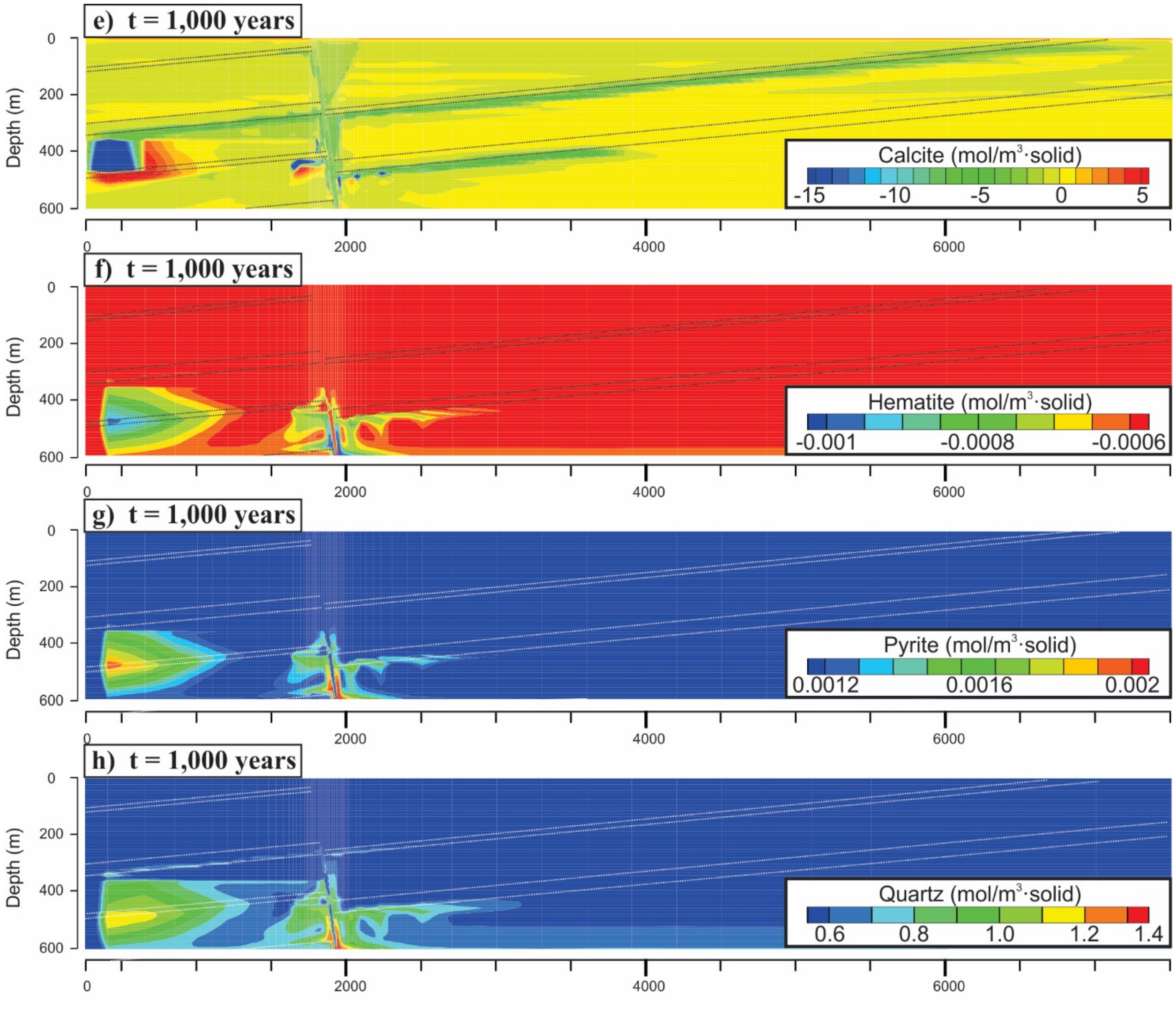

Figure 11 (continued). Two-dimensional distribution of the aqueous species and relevant mineral abundances at t = 1,000 years along the cross-sectional area depicted on Fig. 1b. Note that the right model boundary was cut at 7,500 m from the leftmost margin, to enhance visibility of figures. e) calcite abundance; f) hematite abundance; g) pyrite abundance; h) quartz abundance. Note that hematite abundance values are negative, indicating overall dissolution of the mineral.

also resembles the migrating CO_2 fronts. Additionally, density segregation of the CO_2-bearing fluid caused intense mineral alteration reactions, especially for the areas adjacent to the fault conduit (Fig. 10). The intense alteration caused in these regions is relatively large as displayed in the 2-D space, which could possibly be due to the the size of assigned grid-block (Δx=300m). However, the values associated with the reactions are still reasonable since the lateral boundary (Dirichlet-type) resides in the outskirts of the reaction fronts with no changes and with the minimum grid-block size (Δx=1m).

First, the elevated patterns of Ca^{2+} concentration from calcite dissolution generally followed the subsurface CO_2 migration pattern, concurrently showing the amount of released Ca^{2+} as 0.012 mol/kg·H_2O on average (Fig. 9a and 10a). The calcite dissolution (~ -15 mol/m^3·solid) was especially substantial under the Carmel Fm. at the hanging wall side and the leftmost Navajo Fm. on the footwall side (Fig. 10b). At the same time, calcite precipitation (up to ~ 5.0 mol/m^3·solid) occurred beneath the regions with intensive dissolution. Accordingly, it is implied that strong CO_2 sources and the anticlinally-trapped CO_2 can lead to a mineralization of calcite under these CO_2-rich zones, by pH buffering resulting from silicate and carbonate dissolution.

Fig. 10d displays locations where hematite dissolution was intensified (~ -0.001 mol/m^3·solid), which is adjacent to the bottom part of the fault conduit. Particularly, the strongest dissolution of hematite was observed near the damage zone of the fault where the pH was observed at the lowest (pH=5.0; Fig. 9g). Due to the hematite dissolution compensated by pyrite precipitation, change in Fe^{2+} occurred at ~ 6.0×10^{-15} mol/kg·H_2O in the ambient fluid, which was similar to the observation from the 1-D modeling result shown in Fig. 8d. Hematite dissolution and pyrite precipitation revealed approximately 2:1 exchange ratio of Fe between the two minerals (Fig. 10d and 10f). During this exchange, the SO_4^{2-} concentration in the ambient fluid decreased up to -8.0×10^{-9} mol/kg·H_2O, since the process of pyrite precipitation consumed SO_4^{2-} (Fig. 10e). Decrease in SO_4^{2-} concentration implies possible precipitation of iron-bearing mineral (i.e., pyrite veins) formally observed within this region (Chan et al., 2000; Foxford et al., 1996; Garden et al., 1997).

Distribution of $SiO_{2(aq)}$ concentration showed almost an identical construction to CO_2 saturation, with respect to its local intensities and distribution pattern (Fig. 9a, 10g). An input of the quartzofeldspathic fluid, which resulted from the dissolution of K-feldspar and kaolinite, feeds $SiO_{2(aq)}$ to the ambient fluid (Fig. 10g) and lead to the precipitation of quartz and illite as formerly shown in Figs. 7c and 7d (Fig. 10h). More importantly, the concentration of $SiO_{2(aq)}$ shows strong influence of CO_2 on the footwall side of the fault zone. According to the reactions described above, intense leaching of SiO_2 under the Kayenta and the Carmel Fms. suggests there will be more diagenetic clay and quartz. The results show that the precipitation of quartz and illite will be continued with a sufficient supply of $SiO_{2(aq)}$, K^+, Mg^{2+}, and AlO_2^- provided by the ambient fluid. This indicates a slight growth of relatively stable minerals (quartz and illite) from acid-vulnerable minerals (K-feldspar and kaolinite), which will remain longer in the given chemistry condition.

Overall changes in average mineral abundance throughout the 2-D model were assessed during 1,000 yrs (Fig. 11). According to the model, carbonate minerals continuously dissolved to 900 yrs where the dissolution curves changed its direction towards the precipitation. This effect could be caused by the arrival and escape of CO_2, which have migrated under the Summerville Fm. on the hanging wall side, at the surface (Dirichlet-type) boundary where no more dissolution would occur (Fig. 9a and 10b).

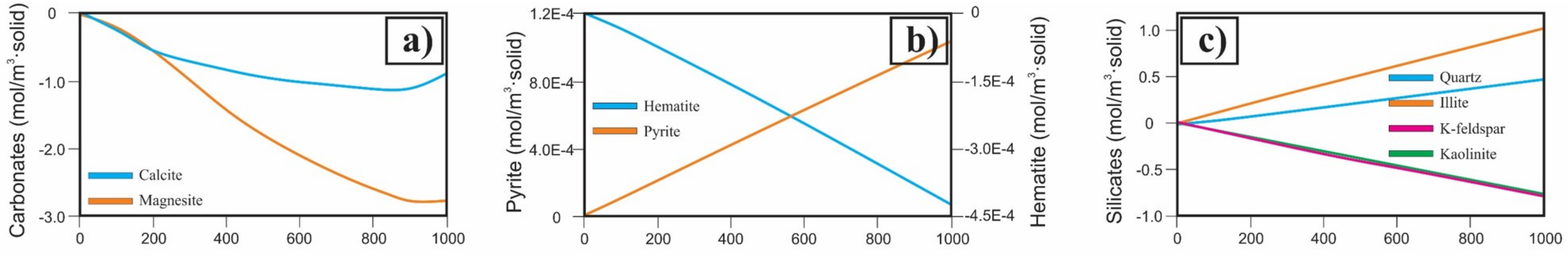

Figure 12. Time-series graphs of average mineral abundance changes throughout the 2-D model during the 1,000-year simulation period. a) calcite and magnesite; b) hematite and pyrite; c) quart, illite, K-feldspar and kaolinite. Note that the y-axes of graphs vary by each mineral species.

However, the continuous dissolution and precipitation of Fe-bearing and silicate minerals under the same conditions suggest that their dissolution and precipitation primarily occurred at the subsurface where there is no significant boundary effect as seen in Figs. 10d, 10f, and 10h.

5.2.3. Changes in Alterations Observed Adjacent to the Fault Conduit

The Roman numeric (I, II, III, IV, and V) and numbers (1, 2, 3, 4, 5, and 6) marked on Fig. 12a indicate monitoring points for both caprocks (Summerville, Carmel, and Kayenta Fms.) and assigned conduit materials along the fault zone where changes of permeability and intrinsic CO_2 in minerals were tracked. A significant increase in permeability of up to 15.7% was observed under caprocks (Zone I to V) while changes (1 to 6) in the fault conduit were limited to the value of 0.062 % (Fig. 12b and 12c).

The maximum degree of change in permeability was observed at Zone III situated approximately 100 m away from the center of the fault conduit under the Kayenta Fm. on the footwall side; here, the maximum reduction of pH was also observed as depicted in Fig. 9g. By comparing permeability changes at Zone III (~15.7%) on the footwall side and Zone V (~2.8%) on the hanging wall side, it is distinct that the significant reactions are manifested on the footwall where CO_2 is trapped under the anticlinal structure.

The intrinsic CO_2 indicates that the inherent amount of carbonate in each assigned grid-block medium (Fig. 12d and 12e). When the CO_2-laden fluid contacts a medium, this intrinsic CO_2 will vary with alteration induced by the fluid and thus releasing carbonate from minerals. In the model, overall intrinsic CO_2 decreased up to -1.19% and -0.36% at the caprocks and conduit from initial rock compositions, respectively.

However, changes of intrinsic CO_2 in Zones I to V remained similar to the conduit measuring points (Zone 1 to 6) except Zone III, while the permeability under the caprocks changed more than two orders of magnitude compared to the conduit. To ascertain the cause of these large differences in permeability changes, calcite precipitation pattern, being the most altered mineral (~ -15 $mol/m^3 \cdot solid$) was needed to be taken into account.

Precipitation and dissolution patterns of calcite adjacent to the fault conduit at t = 1,000 yrs is displayed in Fig. 12a, following the same resolution of magnification that was formerly observed in Fig. 9. The observed distribution of dissolution corresponds to the changes in permeability and intrinsic CO_2. For instance, the most altered Zone III is affected by the strong dissolution that occurred under the Kayenta Fm., resulting in an intensive permeability increase. In addition, Zones 1 and 5 show an increase of intrinsic CO_2 after 400 yrs with changes of -1 ~ 0 $mol/m^3 \cdot solid$, which is a slightly lower value of dissolution than the ambient area. Although Zone 4 is located on the similar anticlinal structure along the fault conduit, it does not, however, show the same trend of calcite precipitation as found in Zones 1 and 5, since the lateral boundary of the Navajo Fm. feeds the aquifer continuously.

Thus, it is implied that the permeability reduction that occurred at Zones 1 and 5 is probably due to the Ca^{2+}-rich back-flux resulting from intensive alterations near the zones, causing re-precipitation of carbonate species to fill up the pores.

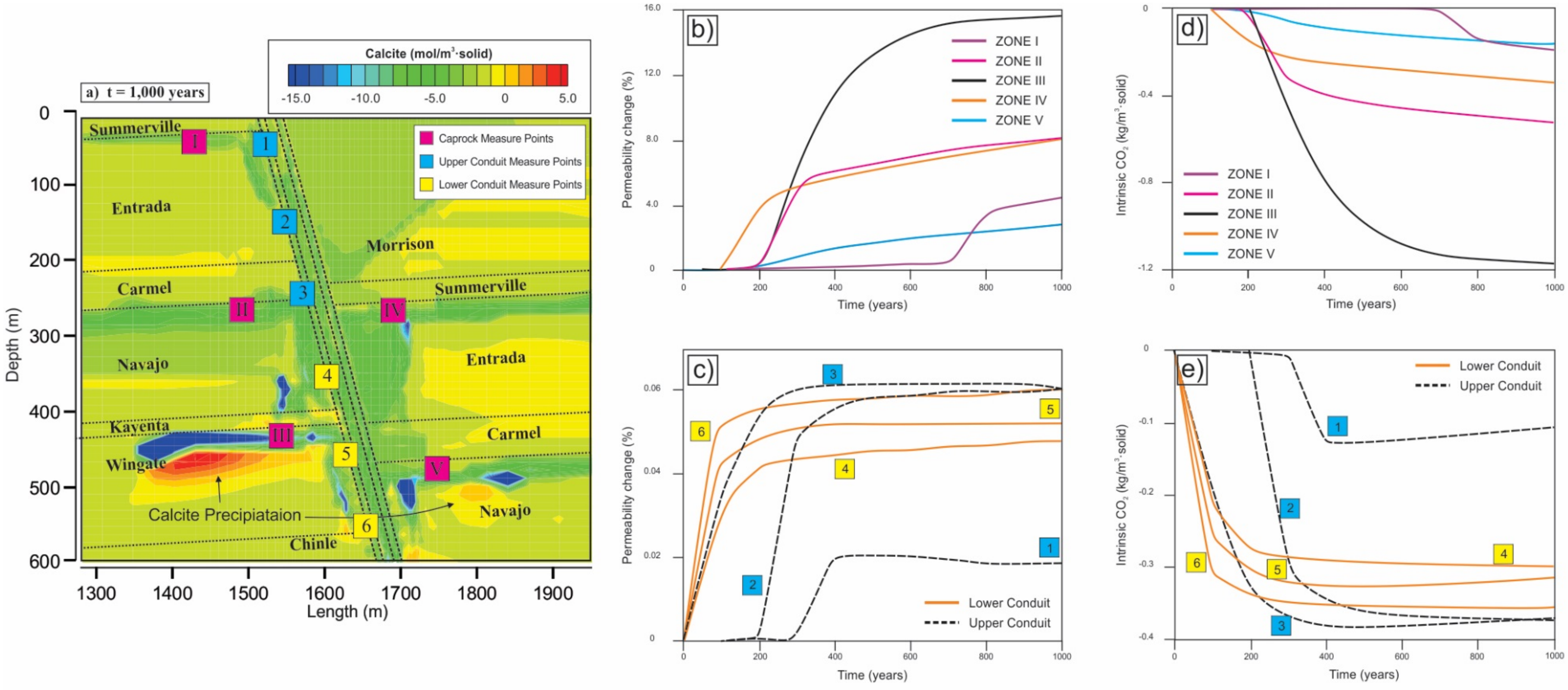

Figure 13. a) Degree of alteration with respect to calcite t = 1,000 years of the simulated period. Permeability changes of: b) zone I to V under low-k caprocks; c) zone 1 to 6 along the fault damage zone. Changes in the amount of mineralized CO_2 of: d) zone I to V under low-k caprocks; e) zone 1 to 6 along the fault damage zone. Note the unit of minerals is molar change in unit volume of the grid-block solid.

6. Discussions: CO_2-induced Changes in the Leaking Fault Zone

6.1. Fluid-assisted Diagenetic Sealing Process in the Fault Zone

Prolonged displacement of the CO_2-laden fluid in hypothetical storage reservoirs through formations and geologic imperfections showed two concomitant mechanisms in former studies: 1) Self-enhancing, which promotes the fluid flux to be enlarged by alteration of formation rocks (Gaus, 2010; Gherardi et al., 2007; Shiraki and Dunn, 2000); 2) Self-limiting, which impels the fluid migration by decreased pore spaces (Gherardi et al., 2007; Pruess, 2005). In this study, the consistently increasing amount of dissolved minerals through time (i.e., increased flow availability) in the 1-D and 2-D porous media suggested that the self-enhancing mechanism of fluid migration is occurring in the fault zone (Fig. 12). However, the increase of vertical permeability in the fault conduit medium was only up to 0.06 % on average, resulting only in a minor change in migration considering the original k_v (1.0×10^{-15} m^2). Therefore, the continued precipitation of relatively stable minerals (i.e., quartz and illite) and calcite in the given condition of the fault zone (e.g., $pH < 5.5$; $25.1 < T < 37.6$ °C; 5.84 MPa $< P < 0.14$ MPa) can cause the opposite phenomenon of the self-enhancing mechanism, as previously observed in simulation results. Since these minerals are not easily soluble, the increasing amount of quartz and illite facies predicts the fluid flow will be interrupted when a fault conduit gets filled up by these solids, indicating fluid-assisted diagenetic sealing as one aspect of the self-limiting mechanism.

6.1.1. Silicate Mineral Alterations Induced by CO_2

Growth of quartz and illite as a result of kaolinite and K-feldspar alteration by CO_2-induced reactive fronts were widely observed throughout the models in this study, especially along the fault conduit (Fig. 10f, and 10h). Formerly, precipitation of illite as an alteration product of alumino-silicates (albite and K-feldspar) in numerical models was observed much like the study by André et al. (2007). Field analogues on a fault adjacent to the study area also support model results; strong illite and quartz precipitation observed under the Kayenta Fm. on the footwall side showed similar localization of extensive chert cementation replacing limestone deposit on the crest of anticlinal structure in the Moab Fault zone (Fig. 10h) (Haszeldine et al., 2005).

The unconfined Paleocene fluid activity (i.e., fault-controlled fluid migration) was suggested as a cause of this silicate mineral enrichment along the Moab Fault zone (Solum et al., 2010). In addition, Solum et al. (2005) noted that more than 50% of neocrystallized illite is formed largely due to the fault-related fluid migration. The gouges and the damage zone in the Moab Fault was enriched up to 40% and up to 50% in $1M_d$ illite with respect to the protolith, respectively (Solum et al., 2005). Furthermore, quartz overgrowths on hematite grain in samples of the Navajo Sandstone have been previously reported (Beitler et al., 2005). Illite in the region was indicated as the alteration product of kaolinite, while kaolinite and illite occur as intergranular or intragranular pore linings (Beitler et al., 2005).

Diagenetic clays and quartz as a consequence of this alteration can promote the fluid-assisted fault healing processes (Evans and Chester, 1995; Tenthorey et al., 2003). Permeability of the fault conduit can be significantly controlled by the clay fraction until it reaches 25 to 40 vol. % (Faulkner et al., 2010; Takahashi et al., 2007). Meanwhile, altered feldspars producing phyllosilicates have been associated with volume-loss, reduced permeability and rheological strength of a fault zone (Bense et al., 2013; Evans, 1988; Goddard and Evans, 1995; Wintsch et al., 1995). The dissolved and re-precipitated quartz has been indicated as a cause of significant permeability reduction of fault cores, by field and laboratory investigations (Chester and Logan, 1986; Evans, 1988). Furthermore, Haszeldine et al. (2005) suggested that the decrease of SiO_2 solubility associated with CO_2 exsolution and pressure decline near the surface is one of the reasons that cause the self-sealing of a fault zone.

Although the chemical affinity of clay-forming aqueous species can be greatly lowered when a layer of clay coating is developed (Zhu, 2005), the irreversibility of silicate reactions suggests that these alteration products (i.e., quartz and illite) will remain stable in the fault conduit (Langmuir et al., 1997). Furthermore, CO_2-promoted silicate mineral alteration is significantly faster than the natural dissolution of silicate minerals in a formation. In-situ dissolution rates calculated formerly for K-feldspar and plagioclase in the Navajo Sandstone were 10^{-19} and 10^{-16} $mol \cdot m^{-2}s^{-1}$, respectively (Zhu, 2005). When compared to the model-estimated dissolution rates with an avg. value of 6.3×10^{-12} $mol \cdot m^{-2}s^{-1}$, it is indicated that the input of CO_2 plays a key role in silicic mineral alterations in the region, even though the thermodynamic constants were exaggerated in the model, e.g., Wigley et al. (2013a).

6.1.2. Switching of Travertine Deposit Locations and Subsurface Calcite Precipitations

Travertine deposit locations on the LGW and SW faults have been switched due to changes in properties of fault hydrologic parameters (Burnside, 2010). This switching mechanisms of travertine mounds were formerly suggested as i) closure of pathways by precipitation of minerals, ii) local and remote seismic activities, and iii) climate related changes (Burnside et al., 2013). In addition, volumetric variations of travertine were said to be due to the post-glacial isostatic unloading (Kampman et al., 2012). However, surface deposition of travertine by strong CO_2 flux from overlapping leakage sources can cause slight closure of the fault conduit with assistance from the aforementioned silicate mineral alterations in terms of a self-limiting process, which can lead to a switching of travertine deposition. Episodicity of this alternating sequence of travertine deposition (i.e., self-limiting) and fault opening (i.e., self-enhancing) by over-pressurized fluid is described in Frery et al. (2015), showing repeated cycles of fault opening and sealing.

The observed precipitation of calcite under the Kayenta and Carmel Fms. on the footwall side and on the hanging wall side, respectively, indicates a possible deposition of carbonate minerals in subsurface (Fig. 12a). In addition, abrupt changes in the curvature of calcite (dissolution curve) indicate precipitation of the mineral, suggesting that the system transits toward the supersaturated condition with respect to calcite due to the prolonged influx of CO_2 (Fig. 11a).

From the drilling operation of the Crystal Geyser, it was revealed that several portions of shale and sandstone formations (approx. 236 m; 588 m; and near surface) along the wellbore accommodates calcite deposits (Williams, 2005)(Glen Ruby #1-X Well Log). This discovery supports the plausibility of precipitation, where inhibition of formation-parallel flow to the fault is possible from the assistance of silicate mineral precipitations by decreased pore spaces (Fig. 10h and 12a); this was also observed in a series of simulations in this study. On a large time scale, this will induce insufficient groundwater input to the fault zone, which may cause formation dry-out and salt precipitation, interrupting CO_2-laden fluid in the fault conduit, e.g., (Pruess and Müller, 2009). However, if dissolution of the deposit occurs by the switching of pathways for CO_2-bearing reactive fluid due to changes in remote stress, e.g., regional seismicity, this can lead to a development of a large sinkhole, e.g., Billi et al. (2007).

The term “inactive travertine” indicates that the mounds are no longer being deposited. The inactive travertine mounds in the study area were constrained to an area of high fracture density along the LGW fault particularly where the two main fault traces lie close together (Jung et al., 2014). At the SW fault, both active and inactive travertine deposits that were relatively smaller in size were restricted to the northern footwall (Fig. 2b). Large volumes of inactive travertines were intersected by the northern trace of the SW fault, but relatively small volumes of both inactive travertines and active travertines associated with CO_2 springs were even further north of the SW fault. This structural relation implies that the intensity of a leakage is highly dependent on intrinsic parameters relying on structural features of the fault rather than the characteristics of CO_2 on the surface. Correlations among travertine deposits, CO_2 flux anomalies with topographical differences and U-Th age of travertine showed little significance (Burnside et al., 2013); the only notable correlation was between CO_2 flux and both the size of ancient travertine deposits and their distances from fault traces. Thus, location switching is mainly due to the changes of fault/fracture properties observed in this study.

6.2. Physicochemical Aspects of the Cold-Water Geyser System

Several cold-water geysers and springs reside in the Green River area (Fig. 1 and 3). Specifically, the largest CO_2-driven cold-water geyser, the Crystal geyser (Glen Ruby #1-X well), has periodically erupted since it was drilled in the mid-1930’s, showing multiple transitions of eruption patterns (eruption intervals and duration). In the 1970’s, the geyser eruption was unimodal, consistently having an interval of 4 hr 15 min (Baer and Rigby, 1978). In 2005, Gouveia and Friedmann (2006) attached pressure and temperature sensors to the hole at the surface. After capturing 140 eruptions over 76 days, they revealed that the eruption patterns transited from a unimodal to a bimodal eruption with longer eruption durations. Further continuous monitoring showed that the geyser eruption pattern changed again from bimodal to unimodal patterns between 2011 and 2012 with distinctly long eruption duration (e.g., over 20 hours) (Han et al., 2013; Watson et al., 2014).

McKnight (1940) has reported that the Glen Ruby #1-X well was drilled down to 863 m, indicating that the Crystal Geyser can be fed by various aquifers underneath (Table 1). However, recent study on the geyser using inverse modeling suggests that the wellbore is fed by 53 to 56 % and 42 to 45 % of water from Navajo and Entrada Sandstone aquifers at the major eruption period, respectively (Watson et al., Submitted Article). According to the CO_2 distribution in the 2-D model, the potential sources of CO_2 for the geyser can also be the Entrada and Navajo Sandstones. Therefore, the alternating eruption periods of MEP and mEP (major and minor eruption periods as in Han et al., 2013) can be driven by switching mechanisms between possible CO_2 accumulation zones and CO_2-charged Navajo and Entrada sandstones.

Likewise, potential CO_2 accumulation zones underneath the Crystal Geyser can affect eruption periods. Since the geyser has been dynamited and capped several times (Glennon, 2005; Murray, 1989; Shipton et al., 2004), chambers associated with these activities can reserve gaseous CO_2 before water recharges the wellbore. Furthermore, the proposed subsurface reactions in this study, e.g., calcite precipitation and associated possible pathway clogging can also cause variations of erupting behavior. Continued influx of quartzofeldspathic and calcic fluid and their precipitation can cause clogging in the geyser as the leakage persists.

6.3. A Cause of Bleaching in the Region and Trace Metal Mobilizations

Bleaching of sandstones is observed on the surface outcrops in the Colorado Plateau; the color of rocks is not uniform with the formations (Beitler et al., 2003; Beitler et al., 2005; Chan et al., 2000; Parry et al., 2004). Controversy about the cause for this bleaching phenomenon still rages unabated. Formerly, the culprit for the broad iron mobilization was suggested as hydrocarbon stored in the region (Beitler et al., 2003; Beitler et al., 2005). However, continuous research has revealed that bleaching is mainly induced by CO_2, without support of such hydrocarbon (Haszeldine et al., 2005; Loope and Kettler, 2015; Wigley et al., 2012).

The simulated results of hematite and pyrite in this study also suggested that the reduction of Fe^{3+} in hematite can be solely driven by CO_2-induced changes in the ambient fluid, without any support of hydrocarbons and additional CH_4 input assigned in the model (Fig. 10d and 10f). To illustrate, the phenomena are mainly due to the dense migration of CO_2 and CO_2-saturated saline fluid, which develop vertical advective and diffusive flow of buoyant CO_2 and gravity current of CO_2-dissolved fluid causing acid-reductive metal mobilization, respectively (Wigley et al., 2013b). The descending CO_2-bearing fluid that formed during the occurrence of density-driven convective mixing can trap the migrating upward flow and then promote the reactions stated above. Moreover, the sustained and linked upslope fluid flow over a long time scale causing persistent exposure of CO_2, has led to an expansive bleaching of the region (Loope and Kettler, 2015; Nielsen et al., 2009; Parry, 2011).

In the meantime, the reducing acid-reactive front, formed by CO_2-saturated fluid, releases and re-deposits Fe ion at the front when the pH is buffered by the ambient fluid (Wigley et al., 2012). A former study observed that linear transects of the Moab fault showed a gradual transition from bleached sandstone to a dense iron mineralization area (Beitler et al., 2005; Chan et al., 2000), indicating *in-situ* re-deposition of iron species. Figs. 10b and 10e suggest that the occurrence of pyrite coeval with the dissolution of hematite by showing concurrent transitions in the models, as interpreted previously by a paragenetic sequence of the two minerals (Garden et al., 2001).

Furthermore, the mobilization of Fe that occurred in simulation results implies an artificial or natural CO_2 leakage site with abundant Mississippi Valley Type (MVT) minerals in the pathways of fluid can exhibit an extensive amount of trace metal release to an aquifer, e.g., (Marcon and Kaszuba, 2015), causing probable pollution of the regional water system. In addition, since CO_2 has an ability to mobilize trace metals without hydrocarbon and CH_4, released Mn, Fe, Ca and pH can be useful markers for leakage indication (Little and Jackson, 2010).

7. Conclusions: Predicted Consequences of Prolonged CO_2 Leakage in the Fault Zone

The LGW and SW fault systems provide unique natural analogues for geologic carbon sequestration with potential CO_2 leakage pathways. Numerical investigations by 1-D and 2-D reactive transport modeling in this study demonstrated that the prolonged migration of subsurface CO_2 to the atmosphere is responsible for quartz and phyllosilicate precipitation, reduction of iron oxide, and carbonate deposition in subsurface environments. A buoyant and highly reactive acid-reductive CO_2 front forms under the regional aquifer conditions and causes these changes.

Diagenetic sealing processes of the LGW fault zone involving authigenic clay and quartz growths along the fault conduit observed in the model provide both a direct cause of fault conduit closure. Relatively stable minerals such as quartz and illite in the given condition of the water chemistry and under influence of regional hydrogeologic parameters can survive through the continued history of CO_2-induced changes in the fault conduit. For instance, a crystallized quartz grain is very insoluble and shows one of the smallest dissolution rate (Lasaga, 1984). Bleaching phenomena observed in this study showed that CO_2 is the main cause of Fe mobilization in the region, without influence of methane and/or hydrocarbon sources.

Since the fault zones in the Paradox Basin are mainly formed due to diffuse deformation along the crest of salt dissolution and the uplift of Colorado Plateau (Hecker, 1993), the LGW and SW faults have potential to be activated by a NW-trending extensional stress regime, resulting in increased fault zone permeability. Furthermore, the continuous uplift of the Colorado Plateau can affect the fault fluid migration regime by generating new fractures and faults where the alteration would be concentrated. The uplift mechanism can reduce the remote mean stress, and thus change the fluid pressure, permeability and geometry of a fault subject to failure (Davatzes et al., 2005).

Previously, tectonic events, e.g., magmatic and seismic activities, were suggested as triggers for the release of CO_2 from reservoirs, proposing strong needs for risk assessments (Lewicki et al., 2007). In this case, the oscillating sequence of pore pressure changes by seismicity can produce hydrofractures and thus, a significant leakage of CO_2 can be induced (Nur and Walder, 1992). Furthermore, this oscillation can induce an episodicity of fluid and CO_2 leakage, which is reflected on the field as different travertine ages. However, the study area and western margin of the Colorado plateau have only subtle and ambiguous faulting evidence during the Quaternary, suggesting no recent seismicity in the area.

From this standpoint, diagenetic sealing capacity of faults and caprocks is the key factor for assessing the long-term CO_2 storage secureness. Prolonged alteration of minerals by CO_2 can cause caprocks in the region to be subject to brittle deformations (Lu et al., 2009). Although the modeled fault conduit did not show significant changes in hydrologic properties, alteration of caprocks that caused ~16% increase of permeability can still be subject to sudden fracture generation. Especially, the alteration of silicate minerals observed in this study can significantly affect the caprock properties, principally the brittleness of the formation. In this case, invasion of CO_2 into the water-saturated caprock without fracture can occur with: i) diffusive CO_2 transportation, and ii) capillary infiltration of gaseous CO_2 (Gherardi et al., 2007).

This article observed through the mechanisms that can possibly arise in faults and fractures adjacent to the artificial injection sites. Currently, converging evidences from silicate mineral alteration and carbonate deposits suggest that the fault conduit has a potential to be clogged as a consequence of CO_2-bearing fluid migration. On the contrary, increasing porosity and permeability during the migration of CO_2 shows self-enhancing of fluid through a pathway.

Further studies are required to quantify more precise heterogeneous reactions in the given condition of CO_2 reservoirs and also for non-isothermal effects, which could be adapted onto a series of models. Experimental investigations on in-situ carbonate crystallization and organic chemistry could precisely evaluate the potentials of precipitation.

BIBLIOGRAPHY

[1] Allis, R., Chidsey, T., Gwynn, W., Morgan, C., White, S., Adams, M., Moore, J., 2001. Natural CO_2 reservoirs on the Colorado Plateau and southern Rocky Mountains: Candidates for CO_2 sequestration. Proceedings of the First National Conference on Carbon Sequestration: 14-17.

[2] Anderson, T.R., Fairley, J.P., 2008. Relating permeability to the structural setting of a fault-controlled hydrothermal system in southeast Oregon, USA. Journal of Geophysical Research: Solid Earth, 113(B5).

[3] André, L., Audigane, P., Azaroual, M., Menjoz, A., 2007. Numerical modeling of fluid–rock chemical interactions at the supercritical CO2–liquid interface during CO2 injection into a carbonate reservoir, the Dogger aquifer (Paris Basin, France). Energy conversion and management, 48(6): 1782-1797.

[4] Apps, J., Zheng, L., Zhang, Y., Xu, T., Birkholzer, J., 2010. Evaluation of potential changes in groundwater quality in response to CO_2 leakage from deep geologic storage. Transport in Porous Media, 82(1): 215-246.

[5] Atchley, A.L., Maxwell, R.M., Navarre-Sitchler, A.K., 2013. Human health risk assessment of CO2 leakage into overlying aquifers using a stochastic, geochemical reactive transport approach. Environ Sci Technol, 47(11): 5954-62 10.1021/es400316c.

[6] Baars, D., 1966. Pre-Pennsylvanian Paleotectonics--Key to Basin Evolution and Petroleum Occurrences in Paradox Basin, Utah and Colorado. AAPG Bulletin, 50(10): 2082-2111.

[7] Bachu, S., Gunter, W., Perkins, E., 1994. Aquifer disposal of CO2: hydrodynamic and mineral trapping. Energy conversion and management, 35(4): 269-279.

[8] Baer, J.L., Rigby, J.K., 1978. Geology of the Crystal Geyser and environmental implications of its effluent, Grand County, Utah. Utah Geology, 5(2): 125-130.

[9] Baker, A.A., 1933. Geology and oil possibilities of the Moab district, Grand and San Juan Counties, Utah, US Government Printing Office, US Government Printing Office.

[10] Barbeau, D., 2003. A flexural model for the Paradox Basin: implications for the tectonics of the Ancestral Rocky Mountains. Basin Research, 15(1): 97-115 10.1046/j.1365-2117.2003.00194.x.

[11] Barth, J.A., 2012. Crystal Geyser, Utah: Active Travertine Deposits of a Cold-water Carbon Dioxide-driven Geyser and Related Ancient Deposits of the Little Grand Wash Fault, University of Houston.

[12] Barton, J.R., Fuhriman, D.K., 1973. Crystal Geyser Project: A Study of Some Alternative Methods for Eliminating the Salt Contribution of Crystal Geyser from the Green River. Center for Environmental Studies, Brigham Young University.

[13] Bear, J., 1972. Dynamics of fluids in porous media. Courier Corporation.

[14] Beitler, B., Chan, M.A., Parry, W.T., 2003. Bleaching of Jurassic Navajo sandstone on Colorado Plateau Laramide highs: Evidence of exhumed hydrocarbon supergiants? Geology, 31(12): 1041-1044.

[15] Beitler, B., Parry, W.T., Chan, M.A., 2005. Fingerprints of Fluid Flow: Chemical Diagenetic History of the Jurassic Navajo Sandstone, Southern Utah, U.S.A. Journal of Sedimentary Research, 75(4): 547-561 10.2110/jsr.2005.045.

[16] Bense, V.F., Gleeson, T., Loveless, S.E., Bour, O., Scibek, J., 2013. Fault zone hydrogeology. Earth-Science Reviews, 127: 171-192 10.1016/j.earscirev.2013.09.008.

[17] Billi, A., Valle, A., Brilli, M., Faccenna, C., Funiciello, R., 2007. Fracture-controlled fluid circulation and dissolutional weathering in sinkhole-prone carbonate rocks from central Italy. Journal of Structural Geology, 29(3): 385-395.

[18] Brandt, C., 1987. The oil and gas potential of the Escalante known geologic structure. Open-File Report 102, Utah Geological Survey; Natural Resources.

[19] Burnside, N.M., 2010. U-Th dating of travertines on the Colorado Plateau: implications for the leakage of geologically stored CO2, University of Glasgow.

[20] Burnside, N.M., Shipton, Z.K., Dockrill, B., Ellam, R.M., 2013. Man-made versus natural CO_2 leakage: A 400 k.y. history of an analogue for engineered geological storage of CO2. Geology, 41(4): 471-474 10.1130/g33738.1.

[21] Busigny, V., Dauphas, N., 2007. Tracing paleofluid circulations using iron isotope: A study of hematite and goethite concretions from the Navajo Sandstone (Utah, USA). Earth and Planetary Science Letters, 254(3-4): 272-287.

[22] Caine, J.S., Evans, J. P., Forster, C. B., 1996. Fault zone architecture and permeability structure. Geology, 24(11): 1025-1028.

[23] Campbell, A.J., Baer, L.J., 1978. Little Grand Wash Fault–Crystal Geyser Area (CO2 Gas), T. 21-22 S., R. 15-17 E., Grand and Emery Counties, Utah.

[24] Cappa, J.A., Rice, D.D., 1995. Carbon dioxide in Mississippian rocks of the Paradox Basin and adjacent areas, Colorado, Utah, New Mexico, and Arizona.

[25] Carroll, S., Hao, Y., Aines, R., 2009. Geochemical detection of carbon dioxide in dilute aquifers. Geochemical transactions, 10(1): 4.

[26] Chan, M.A., Parry, W., Bowman, J., 2000. Diagenetic hematite and manganese oxides and fault-related fluid flow in Jurassic sandstones, southeastern Utah. AAPG Bulletin, 84(9): 1281-1310.

[27] Chang, K.W., Minkoff, S.E., Bryant, S.L., 2008. Modeling leakage through faults of CO2 stored in an aquifer, SPE Annual Technical Conference and Exhibition. Society of Petroleum Engineers.

[28] Chester, F., Logan, J., 1986. Implications for mechanical properties of brittle faults from observations of the Punchbowl fault zone, California. Pure and applied geophysics, 124(1-2): 79-106.

[29] Chiaramonte, L., Zoback, M.D., Friedmann, J., Stamp, V., 2008. Seal integrity and feasibility of CO2 sequestration in the Teapot Dome EOR pilot: geomechanical site characterization. Environmental Geology, 54(8): 1667-1675.

[30] Corey, A.T., 1954. The interrelation between gas and oil relative permeabilities. Producers monthly, 19(1): 38-41.

[31] Cullers, R.L., 1995. The controls on the major-and trace-element evolution of shales, siltstones and sandstones of Ordovician to Tertiary age in the Wet Mountains region, Colorado, USA. Chemical Geology, 123(1): 107-131.

[32] Czernichowski-Lauriol, I., Sanjuan, B., Rochelle, C., Bateman, K., Pearce, J., Blackwell, P., 1996. Analysis of the geochemical aspects of the underground disposal of CO_2.

[33] Davatzes, N., Aydin, A., 2003. Overprinting faulting mechanisms in high porosity sandstones of SE Utah. Journal of Structural Geology, 25(11): 1795-1813.

[34] Davatzes, N.C., Eichhubl, P., Aydin, A., 2005. Structural evolution of fault zones in sandstone by multiple deformation mechanisms: Moab fault, southeast Utah. Geological Society of America Bulletin, 117(1): 135 10.1130/b25473.1.

[35] Dickinson, W.R., Lawton, T.F., 2003. Sequential intercontinental suturing as the ultimate control for Pennsylvanian Ancestral Rocky Mountains deformation. Geology, 31(7): 609-612.
Dobbin, C.E., 1969. Geology of natural gases rich in helium, nitrogen, carbon dioxide, and hydrogen sulfide.

[36] Dockrill, B., 2005. Understanding leakage from a fault-sealed CO2 reservoir in East-Central Utah: a natural analogue applicable to CO_2 storage. Ph.D. Thesis, University of Dublin, Trinity College.

[37] Dockrill, B., Shipton, Z.K., 2010. Structural controls on leakage from a natural CO_2 geologic storage site: Central Utah, U.S.A. Journal of Structural Geology, 32(11): 1768-1782 10.1016/j.jsg.2010.01.007.

[38] Doelling, H., 1994. Tufa deposits in west Grand County. County Survey Notes Utah Geological Survey: 2-3.

[39] Doelling, H.H., 1985. Geology of Arches National Park (Utah). Utah Geological & Mineral Survey.

[40] Doelling, H.H., Oviatt, C.G., Huntoon, P.W., 1988. Salt Deformation in the Paradox Region, Utah (B-122).

[41] Duan, Z., Sun, R., Zhu, C., Chou, I.-M., 2006. An improved model for the calculation of CO_2 solubility in aqueous solutions containing Na^+, K^+, Ca^{2+}, Mg^{2+}, Cl^-, and SO_4^{2-}. Marine Chemistry, 98(2): 131-139.

[42] Eichhubl, P., Davatzes, N.C., Becker, S.P., 2009. Structural and diagenetic control of fluid migration and cementation along the Moab fault, Utah. AAPG Bulletin, 93(5): 653-681.

[43] Ennis-King, J., Paterson, L., 2002. Engineering aspects of geological sequestration of carbon dioxide, SPE Asia Pacific Oil and Gas Conference and Exhibition. Society of Petroleum Engineers.

[44] Evans, J.P., 1988. Deformation mechanisms in granitic rocks at shallow crustal levels. Journal of Structural Geology, 10(5): 437-443.

[45] Evans, J.P., Chester, F.M., 1995. Fluid-rock interaction in faults of the San Andreas system: Inferences from San Gabriel fault rock geochemistry and microstructures. Journal of Geophysical Research: Solid Earth, 100(B7): 13007-13020.

[46] Faulkner, D.R., Jackson, C.A.L., Lunn, R.J., Schlische, R.W., Shipton, Z.K., Wibberley, C.A.J., Withjack, M.O., 2010. A review of recent developments concerning the structure, mechanics and fluid flow properties of fault zones. Journal of Structural Geology, 32(11): 1557-1575 10.1016/j.jsg.2010.06.009.

[47] Foxford, K.A., Garden, I.R., Guscott, S.C., Burley, S.D., Lewis, J.J.M., Walsh, J.J., Watterson, J., 1996. The Field Geology of the Moab Fault, Geology and Resources of the Paradox Basin.

[48] Foxford, K.A., Walsh, J.J., Watterson, J., Garden, I.R., Guscott, S.C., Burley, S.D., 1998. Structure and content of the Moab fault zone, Utah, USA, and its implications for fault seal prediction. Geological Society, London, Special Publications, 147(1): 87-103.

[49] Frery, E., Gratier, J.-P., Ellouz-Zimmerman, N., Loiselet, C., Braun, J., Deschamps, P., Blamart, D., Hamelin, B., Swennen, R., 2015. Evolution of fault permeability during episodic fluid circulation: Evidence for the effects of fluid–rock interactions from travertine studies (Utah–USA). Tectonophysics, 651: 121-137.

[50] Garcia, J.E., 2001. Density of aqueous solutions of CO_2. Lawrence Berkeley National Laboratory.

[51] Garden, I., Guscott, S., Burley, S., Foxford, K., Walsh, J., Marshall, J., 2001. An exhumed palaeo-hydrocarbon migration fairway in a faulted carrier system, Entrada Sandstone of SE Utah, USA. Geofluids, 1(3): 195-213.

[52] Garden, I., Guscott, S., Foxford, K., Burley, S., Walsh, J., Watterson, J., 1997. An exhumed fill and spill hydrocarbon fairway in the Entrada sandstone of the Moab anticline, Utah. Migration and interaction in sedimentary basins and orogenic belts: Geofluids, 2: 287-290.

[53] Gaus, I., 2010. Role and impact of CO2–rock interactions during CO2 storage in sedimentary rocks. International Journal of Greenhouse Gas Control, 4(1): 73-89.

[54] Gerling, C., 1983. McElmo dome Leadville carbon dioxide field, Colorado.

[55] Gherardi, F., Xu, T., Pruess, K., 2007. Numerical modeling of self-limiting and self-enhancing caprock alteration induced by CO2 storage in a depleted gas reservoir. Chemical Geology, 244(1-2): 103-129 10.1016/j.chemgeo.2007.06.009.

[56] Gilfillan, S.M.V., Ballentine, C.J., Holland, G., Blagburn, D., Lollar, B.S., Stevens, S., Schoell, M., Cassidy, M., 2008. The noble gas geochemistry of natural CO2 gas reservoirs from the Colorado Plateau and Rocky Mountain provinces, USA. Geochimica et Cosmochimica Acta, 72(4): 1174-1198 10.1016/j.gca.2007.10.009.

[57] Glennon, J.A., Pfaff, R. M., 2005. The Operation and Geography of Carbon Dioxide-Driven, Cold-Water “Geysers”. The GOSA Transactions, 9.

[58] Goddard, J.V., Evans, J.P., 1995. Chemical changes and fluid-rock interaction in faults of crystalline thrust sheets, northwestern Wyoming, USA. Journal of Structural Geology, 17(4): 533-547.

[59] Gouveia, F., Friedmann, S., 2006. Timing and prediction of CO2 eruptions from Crystal Geyser, UT. United States. Department of Energy.

[60] Gratier, J.P., Frery, E., Deschamps, P., Royne, A., Renard, F., Dysthe, D., Ellouz-Zimmerman, N., Hamelin, B., 2012. How travertine veins grow from top to bottom and lift the rocks above them: The effect of crystallization force. Geology, 40(11): 1015-1018 10.1130/g33286.1.

[61] Gunter, W., Wiwehar, B., Perkins, E., 1997. Aquifer disposal of CO2-rich greenhouse gases: extension of the time scale of experiment for CO2-sequestering reactions by geochemical modelling. Mineralogy and Petrology, 59(1-2): 121-140.

[62] Han, W.S., Lu, M., McPherson, B.J., Keating, E.H., Moore, J., Park, E., Watson, Z.T., Jung, N.H., 2013. Characteristics of CO2-driven cold-water geyser, Crystal Geyser in Utah:

experimental observation and mechanism analyses. Geofluids, 13(3): 283-297 10.1111/gfl.12018.

[63] Hanshaw, B.B., Hill, G.A., 1969. Geochemistry and hydrodynamics of the Paradox basin region, Utah, Colorado and New Mexico. Chemical Geology, 4(1): 263-294.

[64] Hansley, P.L., 2000. Diagenetic and burial history of the Lower Permian White Rim Sandstone in the tar sand triangle, Paradox basin, southeastern Utah. US Geological Survey Bulletin.

[65] Haszeldine, R., Quinn, O., England, G., Wilkinson, M., Shipton, Z., Evans, J.P., Heath, J., Crossey, L., Ballentine, C., Graham, C., 2005. Natural geochemical analogues for carbon dioxide storage in deep geological porous reservoirs, a United Kingdom perspective. Oil & Gas Science and Technology, 60(1): 33-49.

[66] Heath, J., 2004. Hydrogeochemical characterization of leaking carbon dioxide-charged fault zones in east-central Utah, M.S. Thesis, Utah State University.

[67] Heath, J.E., Lachmar, T.E., Evans, J.P., Kolesar, P.T., Williams, A.P., 2009. Hydrogeochemical Characterization of Leaking, Carbon Dioxide-Charged Fault Zones in East-Central Utah, With Implications for Geologic Carbon Storage. Carbon Sequestration and Its Role in the Global Carbon Cycle: 147-158.

[68] Hecker, S., 1993. Quaternary tectonics of Utah with emphasis on earthquake-hazard characterization. Utah Geological Survey.

[69] Helgeson, H.C., Kirkham, D.H., Flowers, G.C., 1981. Theoretical prediction of the thermodynamic behavior of aqueous electrolytes by high pressures and temperatures; IV, Calculation of activity coefficients, osmotic coefficients, and apparent molal and standard and relative partial molal properties to 600 degrees C and 5kb. American Journal of Science, 281(10): 1249-1516.

[70] Hintze, L.F., 1993. Geologic history of Utah, Special Publication 7, 202 p, Dept. of Geology, Brigham Young University.

[71] Hite, R.J., 1968. Salt deposits of the Paradox Basin, southeast Utah and southwest Colorado. Geological Society of America Special Papers, 88: 319-330.

[72] Hite, R.J., Anders, D.E., Ging, T.G., 1984. Organic-rich source rocks of Pennsylvanian age in the paradox basin of Utah and Colorado. Hydrocarbon Source Rocks of the Greater Rocky Mountain Region.

[73] Hite, R.J., Gere, W., 1958. Potash deposits of the Paradox basin. Guidebook to the Geology of the Paradox Basin, Intermountain Association of Petroleum Geologists Ninth Annual Field Conference 1958: 221-225

[74] Hood, J.W., Patterson, D.J., 1984. Bedrock aquifers in the northern San Rafael Swell area, Utah, with special emphasis on the Navajo Sandstone. State of Utah Department of Natural Resources Technical Publication, 78. State of Utah, Department of Natural Resources.

[75] Jeandel, E., Battani, A., Sarda, P., 2010. Lessons learned from natural and industrial analogues for storage of carbon dioxide. International Journal of Greenhouse Gas Control, 4(6): 890-909 10.1016/j.ijggc.2010.06.005.

[76] Jung, N.-H., Han, W.S., Han, K., Park, E., 2015. Regional-scale advective, diffusive, and eruptive dynamics of CO2 and brine leakage through faults and wellbores. Journal of Geophysical Research: Solid Earth, 120(5): 3003-3025 10.1002/2014jb011722.

[77] Jung, N.-H., Han, W.S., Watson, Z.T., Graham, J.P., Kim, K.-Y., 2014. Fault-controlled CO2 leakage from natural reservoirs in the Colorado Plateau, East-Central Utah. Earth and Planetary Science Letters, 403: 358-367 10.1016/j.epsl.2014.07.012.

[78] Kampman, N., Bickle, M.J., Maskell, A., Chapman, H.J., Evans, J.P., Purser, G., Zhou, Z., Schaller, M.F., Gattacceca, J.C., Bertier, P., Chen, F., Turchyn, A.V., Assayag, N., Rochelle, C., Ballentine, C.J., Busch, A., 2014. Drilling and sampling a natural CO2 reservoir: Implications for fluid flow and CO_2-fluid–rock reactions during CO2 migration through the overburden. Chemical Geology, 369: 51-82 10.1016/j.chemgeo.2013.11.015.

[79] Kampman, N., Burnside, N.M., Shipton, Z.K., Chapman, H.J., Nicholl, J.A., Ellam, R.M., Bickle, M.J., 2012. Pulses of carbon dioxide emissions from intracrustal faults following climatic warming. Nature Geoscience, 5(5): 352-358 10.1038/ngeo1451.

[80] Kharaka, Y.K., Ambats, G., Thordsen, J.J., Davis, R.A., 1997. Deep well injection of brine from Paradox Valley, Colorado: Potential major precipitation problems remediated by nanofiltration. Water Resources Research, 33(5): 1013-1020 10.1029/97wr00573.

[81] Kharaka, Y.K., Thordsen, J.J., Kakouros, E., Ambats, G., Herkelrath, W.N., Beers, S.R., Birkholzer, J.T., Apps, J.A., Spycher, N.F., Zheng, L., 2010. Changes in the chemistry of shallow groundwater related to the 2008 injection of CO2 at the ZERT field site, Bozeman, Montana. Environmental Earth Sciences, 60(2): 273-284.

[82] Kling, G.W., Clark, M.A., Wagner, G.N., Compton, H.R., Humphrey, A.M., Devine, J.D., Evans, W.C., Lockwood, J.P., Tuttle, M.L., Koenigsberg, E.J., 1987. The 1986 Lake Nyos gas disaster in Cameroon, West Africa. Science, 236(4798): 169-175.

[83] Knauss, K.G., Johnson, J.W., Steefel, C.I., 2005. Evaluation of the impact of CO2, co-contaminant gas, aqueous fluid and reservoir rock interactions on the geologic sequestration of CO2. Chemical Geology, 217(3-4): 339-350 10.1016/j.chemgeo.2004.12.017.

[84] Kusakabe, M., Ohsumi, T., Aramaki, S., 1989. The Lake Nyos gas disaster: chemical and isotopic evidence in waters and dissolved gases from three Cameroonian crater lakes, Nyos, Monoun and Wum. Journal of volcanology and geothermal research, 39(2): 167-185.

[85] Langmuir, D., Hall, P., Drever, J., 1997. Environmental Geochemistry. Prentice Hall, New Jersey.

[86] Lasaga, A.C., 1984. Chemical kinetics of water-rock interactions. Journal of Geophysical Research: Solid Earth (1978–2012), 89(B6): 4009-4025.

[87] Lewicki, J.L., Birkholzer, J., Tsang, C.-F., 2007. Natural and industrial analogues for leakage of CO2 from storage reservoirs: identification of features, events, and processes and lessons learned. Environmental Geology, 52(3): 457-467.

[88] Little, M.G., Jackson, R.B., 2010. Potential impacts of leakage from deep CO2 geosequestration on overlying freshwater aquifers. Environ Sci Technol, 44(23): 9225-9232.

[89] Loope, D.B., Kettler, R.M., 2015. The footprints of ancient CO2-driven flow systems: Ferrous carbonate concretions below bleached sandstone. Geosphere, 11(3): 943-957 10.1130/ges01094.1.

[90] Lu, C., Sun, Y., Buscheck, T.A., Hao, Y., White, J.A., Chiaramonte, L., 2012. Uncertainty quantification of CO2 leakage through a fault with multiphase and nonisothermal effects. Greenhouse Gases: Science and Technology, 2(6): 445-459.

[91] Lu, J., Wilkinson, M., Haszeldine, R.S., Fallick, A.E., 2009. Long-term performance of a mudrock seal in natural CO2 storage. Geology, 37(1): 35-38.

[92] Lynch, F. L., Lawrence, E. M., Lynton, S. L., 1997. Burial diagenesis of illite/smectite in shales and the origins of authigenic quartz and secondary porosity in sandstones. Geochimica et Cosmochimica Acta, 61(10): 1995-2006.

[93] Marcon, V., Kaszuba, J.P., 2015. Carbon dioxide-brine-rock interactions in a carbonate reservoir capped by shale: Experimental insights regarding the evolution of trace metals. Geochimica et Cosmochimica Acta, 10.1016/j.gca.2015.06.03710.1016/j.gca.2015.06.037.

[94] Marty, B., Jambon, A., 1987. C3He in volatile fluxes from the solid Earth: implications for carbon geodynamics. Earth and Planetary Science Letters, 83(1): 16-26.

[95] Matthäi, S.K., Belayneh, M., 2004. Fluid flow partitioning between fractures and a permeable rock matrix. Geophysical Research Letters, 31(7).

[96] McKnight, E.T., 1940. Geology of the area between Green and Colorado Rivers, Grand and San Juan Counties, Utah. Geological Survey Bulletin, US Government Printing Office, 908

[97] Morrison, S., Parry, W., 1986. Formation of carbonate-sulfate veins associated with copper ore deposits from saline basin brines, Lisbon Valley, Utah; fluid inclusion and isotopic evidence. Economic Geology, 81(8): 1853-1866.

[98] Morey, G. W., Fournier, R. O., Rowe, J. J., 1962. The solubility of quartz in water in the temperature interval from 25 to 300 C. Geochimica et Cosmochimica Acta, 26(10): 1029-1043.

[99] Murray, C., 1989. The cold water geyser of Utah, II: observation of Crystal Geyser. The Geyser Observation and Study Association, 2: 133-9.

[100] Naftz, D., Peterman, Z., Spangler, L., 1997. Using δ^{87}Sr values to identify sources of salinity to a freshwater aquifer, Greater Aneth Oil Field, Utah, USA. Chemical Geology, 141(3): 195-209.

[101] Nagy, K., 1995. Dissolution and precipitation kinetics of sheet silicates. Reviews in Mineralogy and Geochemistry, 31(1): 173-233.

[102] Nielsen, G.B., Chan, M.A., Petersen, E.U., 2009. Diagenetic coloration facies and alteration history of the Jurassic Navajo Sandstone, Zion National Park and vicinity, southwestern Utah, Geology and Geologic Resources and Issues of Western Utah: 67-96.

[103] Nordstrom, D. K., Munoz, J. L., 1986. Geochemical Thermodynamics. Menlo Park, Workingham, Benjamin/Cumming Pub. Co.

[104] Nuccio, V.F., Condon, S.M., 1996. Burial and thermal history of the Paradox Basin, Utah and Colorado, and petroleum potential of the Middle Pennsylvanian Paradox Formation.

[105] Oldenburg, C.M., Lewicki, J.L., 2006. On leakage and seepage of CO2 from geologic storage sites into surface water. Environmental Geology, 50(5): 691-705.

[106] Palandri, J. L., Kharaka, Y. K., 2004. A compilation of rate parameters of water-mineral interaction kinetics for application to geochemical modeling. No. Open-file-2004-1068, US GEOLOGICAL SURVEY MENLO PARK CA; 2004 Mar.

[107] Palandri, J. L., Rosenbauer, R. J., Kharaka, Y. K., 2005. Ferric ion in sediments as a novel CO2 mineral trap: CO2-SO2 reaction with hematite. Applied Geochemistry, 20: 2038-2048.

[108] Parry, W., 2011. Composition, nucleation, and growth of iron oxide concretions. Sedimentary Geology, 233(1): 53-68.

[109] Parry, W.T., Chan, M.A., Beitler, B., 2004. Chemical bleaching indicates episodes of fluid flow in deformation bands in sandstone. AAPG Bulletin, 88(2): 175-191.

[110] Person, M., Baumgartner, L.P., Bos, B., Connolly, J.A.D., Gratier, J.-P., Gueydan, F., Miller, S.A., Rosenberg, C.L., Urai, J.L., Yardley, B.W.D., 2007. Fluids, Geochemical Cycles, and Mass Transport in Fault Zones. In: Handy, M.R., Hirth, G., Hovius, N. (Eds.), Tectonic Faults: Agents of Change on a Dynamic Earth. MIT Press, pp. 403-426.

[111] Pevear, D., Vrolijk, P., Longstaffe, F., 1997. Timing of Moab fault displacement and fluid movement integrated with burial history using radiogenic and stable isotopes. Geofluids II, 97: 42-45.

[112] Pruess, K., 2005. Numerical studies of fluid leakage from a geologic disposal reservoir for CO_2 show self-limiting feedback between fluid flow and heat transfer. Geophysical Research Letters, 32(14): 1-4

[113] Pruess, K., 2007. On CO2 fluid flow and heat transfer behavior in the subsurface, following leakage from a geologic storage reservoir. Environmental Geology, 54(8): 1677-1686

[114] Pruess, K., 2008. Leakage of CO2 from geologic storage: Role of secondary accumulation at shallow depth. International Journal of Greenhouse Gas Control, 2(1): 37-46

[115] Pruess, K., Garcia, J., 2002. Multiphase flow dynamics during CO2 disposal into saline aquifers. Environmental Geology, 42(2-3): 282-295

[116] Pruess, K., Müller, N., 2009. Formation dry-out from CO_2 injection into saline aquifers: 1. Effects of solids precipitation and their mitigation. Water Resources Research, 45(3).

[117] Pruess, K., Xu, T., Apps, J., Garcia, J., 2001. Numerical modeling of aquifer disposal of CO2, SPE/EPA/DOE Exploration and Production Environmental Conference. Society of Petroleum Engineers.

[118] Rau, G., Caldeira, K., 2000. Accelerating carbonate dissolution to sequester carbon dioxide in the ocean: Geochemical implications. Geophys. Res. Lett, 27(2): 225-228.

[119] Reichle, D., Houghton, J., Kane, B., Ekmann, J., 1999. Carbon sequestration research and development. DOE/SC/FE-1, TRN: US200310%%188, Oak Ridge National Lab., TN (US); National Energy Technology Lab., Pittsburgh, PA (US); National Energy Technology Lab., Morgantown, WV (US).

[120] Rinaldi, A.P., Jeanne, P., Rutqvist, J., Cappa, F., Guglielmi, Y., 2014. Effects of fault-zone architecture on earthquake magnitude and gas leakage related to CO2 injection in a multi-layered sedimentary system. Greenhouse Gases: Science and Technology, 4(1): 99-120.

[121] Ross, K., 1998. Cold water geysers in southern Utah. The GOSA Sput, 11(2).

[122] Ruan, H., Gilkes, R., 1995. Dehydroxylation of aluminous goethite: unit cell dimensions, crystal size and surface area. Clays and Clay Minerals, 43(2): 196-211.

[123] Rush, F.E., Whitfield, M., Hart, I., 1982. Regional hydrology of the Green River-Moab area, northwestern Paradox basin, Utah, Geological Survey, Denver, CO (USA). Water Resources Div.

[124] Rutqvist, J., Tsang, C.-F., 2002. A study of caprock hydromechanical changes associated with CO 2 -injection into a brine formation. Environmental Geology, 42(2-3): 296-305 10.1007/s00254-001-0499-2.

[125] Selley, R.C., Sonnenberg, S.A., 2014. Elements of petroleum geology. Academic Press. Shipton, Z.K.E., J.P. , Kirschner, D., Kolesar, P.T., Williams, A.P., Heath, J., 2004. Analysis of CO2 leakage through “low-permeability” faults from natural reservoirs in the Colorado Plateau, east-central Utah. Geological Storage of Carbon Dioxide. Geological Society, London, Special Publications, 233: 43-58.

[126] Shiraki, R., Dunn, T.L., 2000. Experimental study on water–rock interactions during CO2 flooding in the Tensleep Formation, Wyoming, USA. Applied Geochemistry, 15(3): 265-279.

[127] Sibson, R. H., 1990. Conditions for fault-valve behavior. Deformation Mechanisms, Rheology and Tectonics. Geological Society Special Publications, 54: 15-28.

[128] Siirila, E.R., Navarre-Sitchler, A.K., Maxwell, R.M., McCray, J.E., 2012. A quantitative methodology to assess the risks to human health from CO2 leakage into groundwater. Advances in Water Resources, 36: 146-164 10.1016/j.advwatres.2010.11.005.

[129] Smouse, D., 1993. Salt Wash. In: Hill, B.G., Bereskin, S.R. (Eds.), Oil and gas fields of Utah, Utah Geological Association, Salt Lake City, Utah.

[130] Solum, J.G., Davatzes, N.C., Lockner, D.A., 2010. Fault-related clay authigenesis along the Moab Fault: Implications for calculations of fault rock composition and mechanical and hydrologic fault zone properties. Journal of Structural Geology, 32(12): 1899-1911.

[131] Solum, J.G., van der Pluijm, B.A., Peacor, D.R., 2005. Neocrystallization, fabrics and age of clay minerals from an exposure of the Moab Fault, Utah. Journal of Structural Geology, 27(9): 1563-1576.

[132] Spangler, L.E., 1992. Records of wells in sandstone and alluvial aquifers and chemical data for water from selected wells in the Navajo aquifer in the vicinity of the Greater Aneth oil field, San Juan County, Utah. UTAH HYDROLOGIC-DATA REPORT, 47(Open-File Report 92-124).

[133] Spycher, N., Pruess, K., Ennis-King, J., 2003. CO_2-H_2O mixtures in the geological sequestration of CO_2. I. Assessment and calculation of mutual solubilities from 12 to 100 °C and up to 600 bar. Geochimica et Cosmochimica Acta, 67(16): 3015-3031.

[134] Spycher, N.F., Reed, M.H., 1988. Fugacity coefficients of H_2, CO_2, CH_4, H_2O and of H_2O-CO_2-CH_4 mixtures: a virial equation treatment for moderate pressures and temperatures applicable to calculations of hydrothermal boiling. Geochimica et Cosmochimica Acta, 52(3): 739-749.

[135] Steefel, C.I., Lasaga, A.C., 1994. A coupled model for transport of multiple chemical species and kinetic precipitation/dissolution reactions with application to reactive flow in single phase hydrothermal systems. American Journal of Science, 294: 529-592.

[136] Stewart, J.H., Poole, F.G., Wilson, R.F., Cadigan, R., Thordarson, W., Albee, H., 1972. Stratigraphy and origin of the Chinle Formation and related Upper Triassic strata in the Colorado Plateau region. 2330-7102, Geological Survey (US).

[137] Takahashi, M., Mizoguchi, K., Kitamura, K., Masuda, K., 2007. Effects of clay content on the frictional strength and fluid transport property of faults. Journal of Geophysical Research: Solid Earth, 112(B8).

[138] Tenthorey, E., Cox, S.F., Todd, H.F., 2003. Evolution of strength recovery and permeability during fluid–rock reaction in experimental fault zones. Earth and Planetary Science Letters, 206(1): 161-172.

[139] Tester, J.W., Worley, W.G., Robinson, B.A., Grigsby, C.O., Feerer, J.L., 1994. Correlating quartz dissolution kinetics in pure water from 25 to 625 °C. Geochimica et Cosmochimica Acta, 58(11): 2407-2420.

[140] Trimble, L.M., Doelling, H.H., 1978. Geology and uranium-vanadium deposits of the San Rafael River mining area, Emery County, Utah, 113. Utah Geological Survey.

[141] Trudgill, B.D., 2011. Evolution of salt structures in the northern Paradox Basin: controls on evaporite deposition, salt wall growth and supra-salt stratigraphic architecture. Basin Research, 23(2): 208-238

[142] van Genuchten, M.T., 1980. A closed-form equation for predicting the hydraulic conductivity of unsaturated soils. Soil Science Society of America, 44: 892-898

[143] Vrolijk, P., Myers, R., Sweet, M.L., Shipton, Z.K., Dockrill, B., Evans, J.P., Heath, J., Williams, A.P., 2005. Anatomy of reservoir-scale normal faults in central Utah: Stratigraphic controls and implications for fault zone evolution and fluid flow. Field Guides, 6: 261-282.

[144] Walton, P.T., 1955. Wasatch Plateau gas fields, Utah. AAPG Bulletin, 39(4): 385-421.
Wang, S., Jaffe, P.R., 2004. Dissolution of a mineral phase in potable aquifers due to CO_2 releases from deep formations; effect of dissolution kinetics. Energy conversion and management, 45(18): 2833-2848.

[145] Watson, Z.T., Han, W.S., Kampman, N., Graham, J.P., Grundl, T., Keating, E., Han, K., 2016. Periodic Changes in Effluent Chemistry at Crystal Geyser, Green River, Utah. Submitted Article

[146] Watson, Z.T., Han, W.S., Keating, E.H., Jung, N.-H., Lu, M., 2014. Eruption dynamics of CO_2-driven cold-water geysers: Crystal, Tenmile geysers in Utah and Chimayó geyser in New Mexico. Earth and Planetary Science Letters, 408: 272-284.

[147] Weber, J. Weberm R., 2005. Quartz cementation and related sedimentary architecture of the Triassic Solling Formations, Reinhardswald Basin, Germany. Sedimentary Geology, 175(1): 459-477.

[148] White, C.M., Strazisar, B.R., Granite, E.J., Hoffman, J.S., Pennline, H.W., 2003. Separation and capture of CO2 from large stationary sources and sequestration in geological formations—coalbeds and deep saline aquifers. Journal of the Air & Waste Management Association, 53(6): 645-715.

[149] White, S., Allis, R., Moore, J., Chidsey, T., Morgan, C., Gwynn, W., Adams, M., 2005. Simulation of reactive transport of injected CO 2 on the Colorado Plateau, Utah, USA. Chemical Geology, 217(3): 387-405.

[150] Wigley, M., Dubacq, B., Kampman, N., Bickle, M., 2013a. Controls of sluggish, CO2-promoted, hematite and K-feldspar dissolution kinetics in sandstones. Earth and Planetary Science Letters, 362: 76-87.

[151] Wigley, M., Kampman, N., Chapman, H.J., Dubacq, B., Bickle, M.J., 2013b. In situ redeposition of trace metals mobilized by CO_2-charged brines. Geochemistry, Geophysics, Geosystems, 14(5): 1321-1332.

[152] Wigley, M., Kampman, N., Dubacq, B., Bickle, M., 2012. Fluid-mineral reactions and trace metal mobilization in an exhumed natural CO_2 reservoir, Green River, Utah. Geology, 40(6): 555-558.

[153] Wilkinson, M., Gilfillan, S.M.V., Haszeldine, R.S., Ballentine, C.J., 2008. Plumbing the depths: Testing natural tracers of subsurface CO2 origin and migration, Utah. Carbon dioxide sequestration in geological media—State of the science: AAPG Studies, 59: 1-16.

[154] Williams, A.P., 2005. Structural analysis of CO2 leakage through the salt was and little grand was faults from natural reservoirs in the Colorado Plateau, Southeastern Utah, M. S. Thesis, Utah State University.

[155] Wilson, E.J., Friedmann, S.J., Pollak, M.F., 2007. Research for deployment: Incorporating risk, regulation, and liability for carbon capture and sequestration. Environ Sci Technol, 41(17): 5945-5952.

[156] Wintsch, R., Christoffersen, R., Kronenberg, A., 1995. Fluid-rock reaction weakening of fault zones. Journal of Geophysical Research: Solid Earth, 100(B7): 13021-13032.

[157] Wolery, T.J., 1992. EQ3/6: A software package for geochemical modeling of aqueous systems: package overview and installation guide (version 7.0). Lawrence Livermore National Laboratory Livermore, CA.

[158] Xu, T., Apps, J.A., Pruess, K., 2004. Numerical simulation of CO2 disposal by mineral trapping in deep aquifers. Applied Geochemistry, 19(6): 917-936.

[159] Xu, T., Apps, J.A., Pruess, K., 2005. Mineral sequestration of carbon dioxide in a sandstone–shale system. Chemical Geology, 217(3-4): 295-318.

[160] Xu, T., Kharaka, Y.K., Doughty, C., Freifeld, B.M., Daley, T.M., 2010. Reactive transport modeling to study changes in water chemistry induced by CO 2 injection at the Frio-I Brine Pilot. Chemical Geology, 271(3): 153-164.

[161] Xu, T., Sonnenthal, E., Spycher, N., Pruess, K., 2006. TOUGHREACT—A simulation program for non-isothermal multiphase reactive geochemical transport in variably saturated geologic media: Applications to geothermal injectivity and CO2 geological sequestration. Computers & Geosciences, 32(2): 145-165.

[162] Xu, T., White, S. P., Pruess, K., Brimhall, G. H., 2000. Modeling of pyrite oxidation in saturated and unsaturated subsurface flow systems, Transport in porous media, 39(1): 25-56.

[163] Zerai, B., Saylor, B.Z., Matisoff, G., 2006. Computer simulation of CO2 trapped through mineral precipitation in the Rose Run Sandstone, Ohio. Applied Geochemistry, 21(2): 223-240.

[164] Zhu, C., 2005. In situ feldspar dissolution rates in an aquifer. Geochimica et Cosmochimica Acta, 69(6): 1435-1453.

[165] Zoback, M. L., Zoback, M. D., 1989. Tectonic stress field of the continental United States. Geological Society of America Memoirs, 172: 523-540.

[166] Zuluaga, L.F., Fossen, H., Rotevatn, A., 2014. Progressive evolution of deformation band populations during Laramide fault-propagation folding: Navajo Sandstone, San Rafael monocline, Utah, USA. Journal of Structural Geology, 68: 66-81.

APPENDIX A:

The transition state theory describing kinetic rate law

In the models in this study, the rate constant k is dependent on temperature, and is calculated by the Arrhenius equation below:

$$\mathrm{k} = k_{25} exp\left[\frac{-E_a}{R}\left(\frac{1}{T} - \frac{1}{298.15}\right)\right] \qquad (1)$$

where k_{25} is the rate constant at the temperature of 25°C, E_a (J/mol) is the activation energy of the reaction, R (J/K·mol) is the universal gas constant and T is the absolute temperature (K).

The pathways of reaction as precipitation and dissolution are under control of the concentration of hydrogen and hydroxide ions, and reactions which the concentrations of each ion involved are acid and base mechanism, respectively. Hence, the sign of r_n in the eqn. (2) is designated by the following equation including these acid-base mechanisms:

$$r_n = \left[k_{25}^{ne} exp\left[\frac{-E_a^{ne}}{R}\left(\frac{1}{T} - \frac{1}{298.15}\right)\right] + k_{25}^{H^+} exp\left[\frac{-E_a^{H^+}}{R}\left(\frac{1}{T} - \frac{1}{298.15}\right)\right] \cdot a_{H^+}^{n_{H^+}} + k_{25}^{OH^-} exp\left[\frac{-E_a^{OH^-}}{R}\left(\frac{1}{T} - \frac{1}{298.15}\right)\right] a_{OH^-}^{n_{OH^-}}\right] \cdot A_n\left|1 - \Omega_n^{\theta}\right|^{\eta} \qquad (2)$$

where the superscripts ^{ne}, $^{H+}$, and $^{OH-}$ are neutral, acid, and base mechanisms controlling reactions, respectively, and η and θ are experimental coefficients. ‘a’ is the activity of the species in a reaction. Ω_n is the mineral saturation ratio of the equilibrium mineral index ‘n’.

APPENDIX B:

Dissolution and precipitation reactions of the minerals and aqueous species considered in this study models

Mineral	Composition	Reactions
Quartz	SiO_2	$SiO_2 \leftrightarrow SiO_{2(aq)}$
Hematite	Fe_2O_3	$Fe_2O_3 + 4H^+ \leftrightarrow 2H_2O + 0.5O_{2(aq)} + 2Fe^{2+}$
Illite	$K_{0.6}Mg_{0.25}Al_{1.8}(Al_{0.5}Si_{3.5}O_{10})(OH)_2$	$K_{0.6}Mg_{0.25}Al_{1.8}(Al_{0.5}Si_{3.5}O_{10})(OH)_2 \leftrightarrow 1.2H^+ + 0.25Mg^{2+} + 0.6K^+ + 3.5SiO_{2(aq)} + 0.4H_2O + 2.3AlO_2^-$
K-feldspar	$KAlSi_3O_8$	$KAlSi_3O_8 \leftrightarrow K^+ + SiO_{2(aq)} + AlO_2^-$
Kaolinite	$Al_2Si_2O_5(OH)_4$	$Al_2Si_2O_5(OH)_4 \leftrightarrow 2H^+ + 2SiO_{2(aq)} + H_2O + 2AlO_2^-$
Magnesite	$MgCO_3$	$MgCO_3 + H^+ \leftrightarrow Mg^{2+} + HCO_3^-$
Pyrite	FeS_2	$FeS_2 + H_2O + 3.5O_{2(aq)} \leftrightarrow Fe^{2+} + 2H^+ + 2SO4_2^-$
Calcite	$CaCO_3$	$CaCO_3 + H^+ \leftrightarrow Ca^{2+} + HCO_3^-$
Dolomite	$CaMg(CO_3)_2$	$CaMg(CO_3)_2 + H^+ \leftrightarrow Ca^{2+} + Mg^{2+} + 2HCO_3^-$
Chlorite	$Mg_{2.5}Fe_{2.5}Al_2Si_3O_{10}(OH)_8$	$Mg_{2.5}Fe_{2.5}Al_2Si_3O_{10}(OH)_8 + 8H^+ \leftrightarrow 3SiO_{2(aq)} + 2.5Fe^{2+} + 2.5Mg^{2+} + 8H_2O + 2AlO_2^-$
Oligoclase	$CaNa_4Al_6Si_{14}O_{40}$	$CaNa_4Al_6Si_{14}O_{40} \leftrightarrow 4Na^+ + 14SiO_{2(aq)} + Ca^{2+} + 6AlO_2^-$
Albite	$NaAlSi_3O_8$	$NaAlSi_3O_8 \leftrightarrow Na^+ + 3SiO_{2(aq)} + AlO_2^-$
Siderite	$FeCO_3$	$FeCO_3 + H^+ \leftrightarrow Fe^{2+} + HCO_3^-$
Dawsonite	$NaAlCO_3(OH)_2$	$NaAlCO_3(OH)_2 \leftrightarrow H^+ + HCO_3^- + Na^+ + AlO_2^-$
Ankerite	$CaMg_{0.3}Fe_{0.7}(CO_3)_2$	$CaMg_{0.3}Fe_{0.7}(CO_3)_2 + 2H^+ \leftrightarrow 2HCO_3^- + Ca^{2+} + 0.3Mg^{2+} + 0.7Fe^{2+}$
Na-smectite	$Na_{0.290}Mg_{0.26}Al_{1.77}Si_{3.97}O_{10}(OH)_2$	$Na_{0.290}Mg_{0.26}Al_{1.77}Si_{3.97}O_{10}(OH)_2 \leftrightarrow 0.29Na^+ + 0.96H^+ + 0.26Mg^{2+} + 3.97SiO_{2(aq)} + 1.77AlO_2^-$
Ca-smectite	$Ca_{0.145}Mg_{0.26}Al_{1.77}Si_{3.97}O_{10}(OH)$	$Ca_{0.145}Mg_{0.26}Al_{1.77}Si_{3.97}O_{10}(OH) \leftrightarrow 0.52H_2O + 0.145Ca^{2+} + 0.96H^+ + 0.26Mg^{2+} + 3.97SiO_{2(aq)} + 1.77AlO_2^-$

APPENDIX C:

Spearman Rank-Order Correlation coefficients in samples

	TDS	pH	Na^+	K^+	Mg^{2+}	Ca^{2+}	Cl^-	HCO_3^-	SO_4^{2-}
TDS	1	0.72	0.88	0.67	0.11	0.17	0.93	0.14	0.58
pH		1	0.72	0.72	0.74	0.79	0.69	0.77	0.63
Na^+			1	0.71	0.31	0.32	0.84	-0.05	0.37
K^+				1	0.32	0.43	0.66	0.07	0.61
Mg^{2+}					1	0.84	0.14	-0.35	-0.07
Ca^{2+}						1	0.17	-0.17	-0.03
Cl^-							1	-0.05	0.61
HCO_3^-								1	0.05
SO_4^{2-}									1

Spearman Rank-Order Correlation coefficients between TDS, pH, major cations and anions in samples. Values range between -1 and 1 and represented in diagonal direction in order of listed ions. Values > 0.75 are considered as high-positive correlations. Due to limited amount of pH data, 63 samples are collated to calculate pH rank-order, all other correlations were conducted using 98 chemistry data.

APPENDIX D:

Contribution factors of each fluid end-member in the Green River area